Research Square

Preprints are preliminary reports that have not undergone peer review.
They should not be considered conclusive, used to inform clinical practice,
or referenced by the media as validated information.

Comparative Study of Spinor Field Dark Energy Models with Spatial Curvature Constraints

Mahendra Goray

goraymahendra92@gmail.com

S.P. College, Sido Kanhu Murmu University

Research Article

Keywords: Dark energy, Curved geometry, FLRW space-time, Observational constraints, Spinor field cosmology

Posted Date: September 21st, 2026

DOI: https://doi.org/10.21203/rs.3.rs-10926301/v1

License: This work is licensed under a Creative Commons Attribution 4.0 International License.
Read Full License

Additional Declarations: No competing interests reported.

Comparative Study of Spinor Field Dark Energy Models with Spatial Curvature Constraints

Mahendra Goray [a]

[a]Department of Physics, S.P. College, Sido Kanhu Murmu University, Dumka-814101, Jharkhand, India

E-mail: goraymahendra92@gmail.com

Abstract

In this work, we perform a comparative observational analysis of spinor field dark energy (SFDE) models and the standard ΛCDM cosmology using recent cosmological datasets, including Pantheon$^+$, Cosmic Chronometers (CC), DESI DR2 baryon acoustic oscillation measurements, and CMB distance priors in different combined configurations. The analysis is carried out within the framework of FLRW space-time by considering both curved and spatially flat geometries in order to investigate the role of spatial curvature in the evolution of the Universe. To ensure a statistically consistent comparison among models with different numbers of free parameters, we employ the Akaike Information Criterion (AIC) and Bayesian Information Criterion (BIC) in addition to the minimum chi-square analysis. The Markov Chain Monte Carlo (MCMC) results indicate that the spinor-field-based constant-w type dark energy (wSFDE) model provides the most statistically preferred description among the generalized Chaplygin gas (GCG), modified Chaplygin gas (MCG), and standard ΛCDM models for the combined observational datasets. In particular, the wSFDE model exhibits strong sensitivity to spatial curvature, indicating a comparatively stable cosmological evolution in curved geometry. Furthermore, the observational constraints generally become tighter in curved geometry compared with the flat case for all considered cosmological models.

Keywords: Dark energy; Curved geometry, FLRW space-time; Observational constraints; Spinor field cosmology.

I. Introduction

The current epoch of the Universe is undergoing a phase of accelerated expansion. This late-time acceleration, first revealed by observations of Type Ia Supernovae and subsequently confirmed by Cosmic Microwave Background measurements and Baryon Acoustic Oscillation data, indicates the existence of an exotic component with negative pressure, commonly referred to as dark energy [1–9]. The standard cosmological model, the ΛCDM scenario, successfully explains a wide range of observational data. Nevertheless, it suffers from well-known theoretical issues, such as the cosmological constant problem and the coincidence problem [10–14]. Recent observational results from the Dark Energy Spectroscopic Instrument (DESI), particularly its second data release (DR2), have provided the most extensive three-dimensional map of the Universe to date and indicate a possible preference for dynamical dark energy over the ΛCDM model at a confidence level of 2.8σ to 4.2σ [15, 16]. These developments further motivate the exploration of alternative dynamical dark energy models [17, 18].

A wide variety of alternative dark energy models have been proposed in the literature. Among them, scalar field models such as quintessence describe dark energy through a time-dependent field with an evolving equation of state parameter $w(z)$ [14, 19–21]. Parametric approaches like the Chevallier–Polarski–Linder (CPL) model provide a phenomenological description of this evolution [22, 23]. Other physically motivated models include holographic dark energy, which is based on principles of quantum gravity [24–26]. In addition, unified models such as the generalized Chaplygin gas (GCG) [27–29], and its modified version (MCG) [30–32] attempt to describe dark matter and dark energy within a single framework, playing a significant role in the cosmic expansion history. Furthermore, various modified gravity theories have also been developed as alternatives to dark energy [33–35].

While most of these models are traditionally formulated in terms of scalar fields or effective fluids, it is of considerable interest to explore their realization within more fundamental field-theoretic frameworks. In this context, spinor fields provide a natural and well-motivated alternative for describing dark energy dynamics [36–38]. Spinor field models have been shown to reproduce a wide range of cosmological behaviors, including accelerated expansion, by appropriately choosing nonlinear self-interaction terms in the spinor Lagrangian [38]. Interestingly, several dark energy models, including Chaplygin gas and quintessence-type scenarios, can be effectively reconstructed from spinor field dynamics [38, 39]. This correspondence allows one to interpret these phenomenological models within a unified theoretical framework, providing deeper insight into the nature of dark energy. Therefore, studying different dark energy models from a spinor field perspective is not only theoretically appealing but also essential for understanding their underlying physical origin.

In our previous works, we have investigated the generalized Chaplygin gas (GCG), modified Chaplygin gas (MCG), and constant-w type models within the framework of nonlinear spinor fields in the FLRW space-time and constrained them using various observational datasets [40–42]. Although all these models provide a reasonable fit to the data, it remains challenging to identify the most viable spinor field-based dark energy model, primarily because each model has been tested against different combinations of observational datasets. In particular, the constant-w type spinor field dark energy (wSFDE) model was constrained using CC + SDSS + SN + BAO, while the GCG and MCG models were analyzed with OHD + SDSS + SN + BAO and Pantheon$^+$ + CC + DESI DR2 datasets, respectively. This lack of a uniform dataset prevents a consistent and unbiased comparison among the models. Therefore, it is essential to analyze all models within a common observational framework. Such a unified comparison not only enables a fair assessment of their relative performance but also helps to identify models that may be disfavored or ruled out by current observational data.

In this work, we perform a comprehensive comparative study of spinor field dark energy (SFDE) realizations of the GCG, MCG, and wSFDE models, alongside the standard ΛCDM model, in both flat and curved FLRW geometries. All models are constrained using a consistent combination of recent observational datasets, including Pantheon$^+$, cosmic chronometers (CC), DESI DR2, and Cosmic Microwave Background (CMB) data. We employ Markov Chain Monte Carlo (MCMC) techniques to estimate the model parameters and use the χ^2 statistic for likelihood analysis. To further assess the relative performance of the models, we adopt model selection criteria such as the Akaike Information Criterion (AIC) [44] and the Bayesian Information Criterion (BIC) [45]. This approach allows us to systematically compare the viability of different spinor field dark energy models and to determine the model and geometric configuration that is most favored by current observational data.

Our work is organized as follows. The formalism of SFDE models is presented in Section II. Section III is devoted to the observational datasets and the MCMC methodology used to constrain the cosmological parameters. In Section IV, we present and discuss the numerical results. Finally, the main conclusions of the present work are summarized in Section V.

II. Formalism of SFDE

A. Mathematical background

Since the Universe is observed to be approximately homogeneous and isotropic on large scales, we adopt the spherically symmetric Friedmann–Lemaître–Robertson–Walker spacetime (FLRW) line element [46, 47]:

$$ds^2 = dt^2 - a^2(t)\left[\frac{dr^2}{1-kr^2} + r^2 d\theta^2 r^2 \sin^2\theta d\phi^2\right], \tag{1}$$

where $a(t)$ denotes the cosmic scale factor and k represents the spatial curvature parameter. The cases $k = 0$, $k = -1$, and $k = +1$ correspond to flat, open, and closed geometries of the Universe, respectively.

We consider a minimally coupled spinor field interacting with the gravitational field. The corresponding action is written as

$$\mathcal{S} = \int \sqrt{-g}\left[\frac{R}{2\kappa} + L_{\rm sp}\right] d\Omega, \tag{2}$$

where $\kappa = 8\pi G$ is the Einstein gravitational constant, R denotes the Ricci scalar, and $L_{\rm sp}$ represents the spinor field Lagrangian density, given by [39–42]

$$L_{\rm sp} = \frac{\imath}{2}\left[\bar{\psi}\gamma^{\mu}\nabla_{\mu}\psi - \nabla_{\mu}\bar{\psi}\gamma^{\mu}\psi\right] - m_{\rm sp}\bar{\psi}\psi - \lambda F(K). \tag{3}$$

Here, $m_{\rm sp}$ and λ correspond to the spinor mass and the self-interaction coupling constant, respectively. The nonlinear term $F(K)$ is an arbitrary function constructed from the invariants generated by the real bilinear spinor forms. It is important to note that the Dirac equations remain invariant under Lorentz transformations, and the inclusion of the nonlinear self-interaction term preserves this invariance, analogous to the extension employed in $F(R)$ gravity theories. The explicit form of the nonlinear function $F(K)$ can be determined from the corresponding equation of state [39].

Since the spinor field ψ and its complex conjugate $\psi^{\star}$ each possess four independent components, one can construct sixteen independent bilinear quantities from them. These consist of one scalar $S = \bar{\psi}\psi$ ($\bar{\psi} = \psi^{\star}\gamma^{0}$), one pseudo-scalar $P = \imath\bar{\psi}\gamma^{5}\psi$, four vector components $V^{\mu} = \bar{\psi}\gamma^{\mu}\psi$, four pseudo-vector components $A^{\mu} = \bar{\psi}\gamma^{5}\gamma^{\mu}\psi$, and six tensor components $T^{\mu\nu} = \bar{\psi}\sigma^{\mu\nu}\psi$, with

$$\sigma^{\mu\nu} = (\imath/2)[\gamma^{\mu}\gamma^{\nu} - \gamma^{\nu}\gamma^{\mu}]. \tag{4}$$

The corresponding invariants associated with these bilinear forms are defined as $I = S^2$, $J = P^2$, $I_V = V_{\mu}V^{\mu}$, $I_A = A_{\mu}A^{\mu}$ and $I_T = T_{\mu\nu}T^{\mu\nu}$. Using the Fierz identities, these invariants satisfy the relations $I_V = -I_A = I + J$ and $I_T = I - J$. Therefore, owing to the Fierz theorem, the nonlinear term can be expressed in terms of the combinations $K = \{I, J, I + J, I - J\}$ as discussed in [39]. The corresponding spinor field equations are obtained as

$$\imath\gamma^{\mu}\nabla_{\mu}\psi - m_{\rm sp}\psi - \mathcal{D}\psi - \imath\mathcal{G}\gamma^{5}\psi = 0, \tag{5a}$$
$$\imath\nabla_{\mu}\bar{\psi}\gamma^{\mu} + m_{\rm sp}\bar{\psi} + \mathcal{D}\bar{\psi} + \imath\mathcal{G}\bar{\psi}\gamma^{5} = 0, \tag{5b}$$

where

$$\mathcal{D} = 2\lambda F_K S, \quad \mathcal{G} = 2\lambda F_K P, \quad F_K = \frac{dF}{dK}.$$

The components of the energy-momentum tensor (EMT) of the spinor field in the FLRW metric [42],

$$T_0^{\ 0} = m_{\rm sp}S + \lambda F \ = \ \rho_{sp}, \tag{6a}$$
$$T_1^{\ 1} = T_2^{\ 2} = T_3^{\ 3} = -\lambda(2KF_K - F) \ = -p_{sp}, \tag{6b}$$
$$T_3^{\ 1} = \frac{a\cos\theta}{4\sqrt{1-kr^2}}\,A^0, \tag{6c}$$
$$T_1^{\ 0} = \frac{\cot\theta}{4r\sqrt{1-kr^2}}\,A^3, \tag{6d}$$
$$T_2^{\ 0} = -\frac{3}{4}\sqrt{1-kr^2}\,A^3, \tag{6e}$$
$$T_3^{\ 0} = \frac{3}{4}\sqrt{1-kr^2}\,\sin\theta\,A^2 - \frac{1}{2}\cos\theta\,A^1. \tag{6f}$$

Here, ρ_{sp} and p_{sp} denote the total energy density and pressure, respectively.

The components of EMT (6) contain some invariants of the bilinear spinor field. From (5) we deduce a set of equations corresponding to these invariants [42]:

$$\dot{S}_0 + 2\mathcal{G} A_0^0 = 0, \tag{7a}$$

$$\dot{P}_0 - 2\left(m_{sp} + \mathcal{D}\right) A_0^0 = 0, \tag{7b}$$

$$\dot{A}_0^0 + 2\mathcal{G} S_0 + 2\left(m_{sp} + \mathcal{D}\right) P_0 + 2\frac{\sqrt{1-kr^2}}{ar} A_0^1 + \frac{\cot\theta}{ar} A_0^2 = 0, \tag{7c}$$

$$\dot{A}_0^1 + 2\frac{\sqrt{1-kr^2}}{ar} A_0^0 = 0, \tag{7d}$$

$$\dot{A}_0^2 + \frac{\cot\theta}{ar} A_0^0 = 0. \tag{7e}$$

The system of equations (7) is introduced to determine the evolution of the spinor bilinears and, in particular, the dependence of the nonlinear invariant K on the scale factor. The corresponding first integral is

$$P_0^2 - S_0^2 + \left(A_0^0\right)^2 - \left(A_0^1\right)^2 - \left(A_0^2\right)^2 = K_0, \tag{8}$$

where K_0 is a constant. Together with the relations between the bilinears and their rescaled quantities, this allows the invariant K entering the nonlinear spinor-field Lagrangian to be expressed explicitly as a function of the scale factor. The subscript '0' used in the bilinear quantities S_0, P_0, and A_0^μ does not denote an additional tensor index. The quantities with a subscript '0' are related to the corresponding bilinears by $X_0 = a^3 X$, where X represents the corresponding spinor bilinear. Thus, $A_0^\mu = a^3 A^\mu$ for the components appearing in the invariant equations [43].

From Eq. (7), one can explicitly determine the form of the invariant quantity K. Let us first consider the case $K = I = S^2$. Then, from Eq. (7a), we immediately obtain $\dot{S}_0 = 0$, which admits the solution $S = S_0/a^3$, where S_0 is an integration constant. For a massless spinor field and the choice $K = J = P^2$, Eq. (7b) yields $\dot{P}_0 = 0$, with the corresponding solution $P = P_0/a^3$, where P_0 is a constant. In the case $K = I + J$, for a massless spinor field, multiplying Eq. (7a) by S_0 and Eq. (7b) by P_0, and then adding the resulting equations, one obtains $K = I + J = K_0/a^6$. Similarly, for the choice $K = I - J$, subtracting Eq. (7b) multiplied by P_0 from Eq. (7a) multiplied by S_0 gives $K = I - J = K_0/a^6$. Hence, in general, one finds

$$K = \frac{K_0}{a^6}, \tag{9}$$

where, K_0 is constant, and Eq. (9) is valid for both massive and massless spinor fields in the cases $K = \{J,\, I \pm J\}$, whereas for $K = I = S^2$.

Since the off-diagonal components of the Einstein tensor vanish identically, the relations given by Eqs. (6c)–(6f) impose the following constraints on the spinor field components:

$$A^0 = 0, \qquad A^3 = 0, \qquad A^1 = \frac{3}{2}\sqrt{1-kr^2}\,\tan\theta\, A^2. \tag{10}$$

Consequently, the diagonal components of the Einstein field equations take the form

$$2\frac{\ddot{a}}{a} + \left(\frac{\dot{a}^2}{a^2} + \frac{k}{a^2}\right) = -8\pi G\, p_{sp}, \tag{11a}$$

$$3\left(\frac{\dot{a}^2}{a^2} + \frac{k}{a^2}\right) = 8\pi G\, \rho_{sp}. \tag{11b}$$

It should be noted that Eq. (11b) acts as a constraint equation. Using Eq. (11b), Eq. (11a) can be rewritten in the standard acceleration form as

$$\frac{\ddot{a}}{a} = -\frac{4\pi G}{3}\left(\rho_{sp} + 3p_{sp}\right). \tag{12}$$

Furthermore, from Eq. (11b), one obtains

$$\left(\frac{\dot{a}}{a}\right)^2 \equiv H^2 = \frac{8\pi G}{3}\left(m_{\rm sp}S + \lambda F\right) - \frac{k}{a^2}. \tag{13}$$

For a massless spinor field ($m_{\rm sp} = 0$), taking $\rho_{sp} = \lambda F(K)$ from Eq. (6a), the normalized dimensionless Hubble parameter becomes

$$E_{sp}^2 = \frac{H^2}{H_0^2} = \frac{8\pi G}{3H_0^2}\,\rho_{sp} - \frac{k}{a^2H_0^2}, \tag{14}$$

where H and H_0 denote the Hubble parameter and its present-day value, respectively.

B. Dark energy models

Since we consider a massless spinor field in the FLRW space-time, the spinor field energy density and pressure obtained from Eqs. (6a) and (6b) are given by

$$\rho_{sp} = \lambda F(K), \qquad p_{sp} = \lambda\left(2KF_K - F(K)\right), \tag{15}$$

where $F_K = dF/dK$. Using these expressions for the spinor field energy density and pressure, one can determine the nonlinear term $F(K)$ corresponding to a particular equation of state and thereby construct specific dark energy models. In the present work, we construct the spinor field versions of the generalized Chaplygin gas (GCG) [40], modified Chaplygin gas (MCG) [42], and wSFDE models [41].

- **Generalized Chaplygin Gas (GCG):**

  The equation of state (EoS) for the generalized Chaplygin gas model is given by

  $$p_{\rm GCG} = -\frac{A}{\rho_{\rm GCG}^{\alpha}}, \tag{16}$$

  where $A > 0$ is a positive constant and $0 \le \alpha \le 1$.

  Substituting

  $$\rho_{\rm GCG} = \lambda F_{\rm GCG}(K), \qquad p_{\rm GCG} = \lambda\left(2KF_{\rm GCG}{}_K - F_{\rm GCG}(K)\right),$$

  from Eqs. (6) into Eq. (16), we obtain

  $$F_{\rm GCG}(K) = \left(A + \lambda_1 K^{(1+\alpha)/2}\right)^{1/(1+\alpha)}, \tag{17}$$

  where λ_1 is an integration constant, and

  $$F_{\rm GCG}{}_K = \frac{dF_{\rm GCG}}{dK}$$

  Consequently for the massless spinor field, using Eq. (9), the corresponding energy density and pressure become

  $$\rho_{\rm GCG} = \lambda\left(A + \lambda_1(1+z)^{3(1+\alpha)}\right)^{1/(1+\alpha)}, \tag{18a}$$

  $$p_{\rm GCG} = -A\lambda\left(A + \lambda_1(1+z)^{3(1+\alpha)}\right)^{-\alpha/(1+\alpha)}. \tag{18b}$$

  The normalized dimensionless Hubble parameter for the GCG model can be written in the light of Eq. (14) as

  $$E_{\rm GCG}^2 = \frac{8\pi G}{3H_0^2}\rho_{\rm GCG} - \frac{k}{a^2H_0^2}. \tag{19}$$

In terms of the density parameters and redshift, Eq. (19) takes the form

$$E^2_{\rm GCG}(z) = (1-\Omega_{k0})\,\tilde{\rho}_{\rm GCG} + \Omega_{k0}(1+z)^2, \tag{20}$$

where $\tilde{\rho}_{\rm GCG} = \frac{\rho_{\rm GCG}}{\rho_{\rm GCG0}}$, $\Omega_{k0} = -k/H_0^2$, and

$$\Omega_{\rm GCG0} = \frac{8\pi G\rho_{\rm GCG0}}{3H_0^2} = (1-\Omega_{k0}).$$

Here, $\rho_{\rm GCG0}$ denotes the present value of the energy density, defined as

$$\rho_{\rm GCG0} = \lambda\,(A+\lambda_1)^{1/(1+\alpha)}\,. \tag{21}$$

At the present epoch ($z=0$), one has $\tilde{\rho}_{\rm GCG}(0)=1$, which consequently gives

$$E_{\rm GCG}(0) = 1, \qquad H = H_0.$$

- **Modified Chaplygin Gas (MCG):**

The modified Chaplygin gas (MCG) model is characterized by the equation of state

$$p_{\rm MCG} = W\rho_{\rm MCG} - \frac{A}{\rho^{\alpha}_{\rm MCG}}, \tag{22}$$

where W is a constant parameter, $A>0$, and $0\le\alpha\le 1$.

To obtain the corresponding spinor field realization, we substitute

$$\rho_{\rm MCG} = \lambda F_{\rm MCG}(K), \tag{23a}$$
$$p_{\rm MCG} = \lambda\left(2KF_{\rm MCG}{}_K - F_{\rm MCG}(K)\right), \tag{23b}$$

into Eq. (22), where

$$F_{\rm MCG}{}_K = \frac{dF_{\rm MCG}}{dK}.$$

This yields the nonlinear spinor self-interaction term in the form

$$F_{\rm MCG}(K) = \left[\frac{A}{1+W} + \lambda_1 K^{(1+\alpha)(1+W)/2}\right]^{1/(1+\alpha)}, \tag{24}$$

where λ_1 is an integration constant.

Using Eqs. (9), and (23) the corresponding energy density and pressure can be expressed in terms of the redshift parameter z as

$$\rho_{\rm MCG} = \lambda\left[\frac{A}{1+W} + \lambda_1(1+z)^{3(1+\alpha)(1+W)}\right]^{1/(1+\alpha)}, \tag{25a}$$
$$p_{\rm MCG} = \lambda\left[\lambda_1 W(1+z)^{3(1+\alpha)(1+W)} - \frac{A}{1+W}\right]\left[\frac{A}{1+W} + \lambda_1(1+z)^{3(1+\alpha)(1+W)}\right]^{-\alpha/(1+\alpha)}. \tag{25b}$$

Using Eq. (14), the normalized dimensionless Hubble parameter for the MCG model can be written as

$$E^2_{\rm MCG} = \frac{8\pi G}{3H_0^2}\rho_{\rm MCG} - \frac{k}{a^2H_0^2}. \tag{26}$$

Defining the normalized energy density

$$\tilde{\rho}_{\rm MCG} = \frac{\rho_{\rm MCG}}{\rho_{\rm MCG0}},$$

and the present-day curvature density parameter

$$\Omega_{k0} = -\frac{k}{H_0^2},$$

together with

$$\Omega_{\rm MCG0} = \frac{8\pi G\rho_{\rm MCG0}}{3H_0^2} = (1-\Omega_{k0}),$$

where $\rho_{\rm MCG0}$ denotes the present value of the MCG energy density, we obtain

$$\rho_{\rm MCG0} = \lambda\left[\frac{A}{1+W} + \lambda_1\right]^{1/(1+\alpha)}. \tag{27}$$

Consequently, Eq. (26) can be rewritten in the form

$$E^2_{\rm MCG}(z) = (1-\Omega_{k0})\tilde{\rho}_{\rm MCG} + \Omega_{k0}(1+z)^2. \tag{28}$$

At the present epoch ($z=0$), $\tilde{\rho}_{\rm MCG}(0)=1$, which ensures that

$$E_{\rm MCG}(0) = 1, \qquad H(z=0) = H_0.$$

- **wSFDE:**

Since the wSFDE model does not unify dark matter and dark energy, we include an additional pressure less matter component ($p_{\rm m}=0$) in the spinor field wSFDE scenario. Therefore, the total energy density and pressure are given by

$$\rho_{\rm total} = \rho_{\rm m} + \rho_{\rm wSFDE}, \tag{29a}$$

$$p_{\rm total} = p_{\rm wSFDE}, \tag{29b}$$

where $\rho_{\rm wSFDE}$ and $p_{\rm wSFDE}$ denote the wSFDE dark energy density and pressure, respectively. In the light of Eqs. (6a) and (6b), the spinor field contributions can be written as

$$\rho_{\rm wSFDE} = \lambda F_{\rm wSFDE}(K), \qquad p_{\rm wSFDE} = \lambda\left(2KF_{\rm wSFDE}{}_K - F_{\rm wSFDE}(K)\right),$$

with

$$F_{\rm wSFDE}{}_K = \frac{dF_{\rm wSFDE}}{dK}.$$

The nonlinear spinor self-interaction term $F_{\rm wSFDE}(K)$ can be determined using the wSFDE equation of state with constant parameter W,

$$p_{\rm wSFDE} = W\rho_{\rm wSFDE}. \tag{30}$$

Substituting the above expressions for $\rho_{\rm wSFDE}$ and $p_{\rm wSFDE}$ into Eq. (30), we obtain

$$F_{\rm wSFDE}(K) = \lambda_1 K^{(1+W)/2}, \tag{31}$$

where λ_1 is an integration constant.

Consequently, for a massless spinor field, the energy density and pressure become

$$\rho_{\rm wSFDE} = \lambda\lambda_1(1+z)^{3(1+W)}, \tag{32a}$$

$$p_{\rm wSFDE} = \lambda\lambda_1 W(1+z)^{3(1+W)}. \tag{32b}$$

Now, Eq. (14) turn for the wSFDE model with matter component as

$$E^2_{\rm wSFDE}(z) = \Omega_{\rm m0}(1+z)^3 + \Omega_{\rm wSFDE0}\tilde{\rho}_{\rm wSFDE} + \Omega_{\rm k0}(1+z)^2. \tag{33}$$

where, $\tilde{\rho}_{\rm wSFDE} = \rho_{\rm wSFDE}/\rho_{\rm wSFDE0}$ and $\rho_{\rm wSFDE0} = \lambda\lambda_1$. Corresponding present-day wSFDE density parameter

$$\Omega_{\rm wSFDE0} = \frac{8\pi G\rho_{\rm wSFDE0}}{3H_0^2} = (1 - \Omega_{m0} - \Omega_{k0}).$$

The pressureless matter density evolves as

$$\rho_{\rm m} = \rho_{\rm m0}(1+z)^3, \qquad \rho_{\rm m0} = \text{const.} \tag{34}$$

Corresponding matter density parameter can be expressed as

$$\Omega_{\rm m} = \frac{\rho_{\rm m}/\rho_{\rm crit0}}{E^2} = \frac{\Omega_{\rm m0}(1+z)^3}{E^2}, \tag{35a}$$

where $\rho_{\rm m0} = \Omega_{\rm m0}\rho_{\rm crit0}$, and the present critical density is defined as

$$\rho_{\rm crit0} = \frac{3H_0^2}{8\pi G}.$$

At the present epoch ($z = 0$), $\tilde{\rho}_{\rm wSFDE}(0) = 1$, one obtains from Eq. (33)

$$E_{\rm wSFDE}(0) = 1, \qquad H(z=0) = H_0.$$

For comparison with the standard ΛCDM cosmology, the normalized Hubble parameter can be written as

$$E^2_{\Lambda\rm CDM}(z) = \Omega_{\rm m0}(1+z)^3 + \Omega_{\rm k0}(1+z)^2 + \Omega_{\Lambda0}, \tag{36}$$

where

$$\Omega_{\Lambda0} = 1 - \Omega_{\rm m0} - \Omega_{\rm k0}.$$

For the spinor field dark energy models, the effective equation of state parameter is defined by

$$w(z) = \frac{p_{\rm sp}(z)}{\rho_{\rm sp}(z)}, \tag{37}$$

where $p_{\rm sp}$ and $\rho_{\rm sp}$ represent the spinor field pressure and energy density, respectively. The corresponding deceleration parameter is given by

$$q(z) = -\frac{\ddot{a}}{aH^2}, \tag{38}$$

which, in terms of the normalized Hubble parameter $E(z)$, can be rewritten as

$$q(z) = -1 + (1+z)\frac{1}{E(z)}\frac{dE(z)}{dz}. \tag{39}$$

The behaviors of $w(z)$ and $q(z)$ provide important insights into the dynamical evolution of the Universe and allow us to distinguish between different spinor field dark energy scenarios in both flat and curved FLRW geometries.

III. Datasets and Methodology

A. Datasets

To constrain the spinor field dark energy models along with the ΛCDM model within the FLRW framework for both curved and flat geometries, we employ a combination of recent cosmological observations. The analysis is performed using a joint likelihood constructed from Cosmic Chronometers (CC), Type Ia Supernovae (Pantheon$^+$: PP), Baryon Acoustic Oscillation (BAO) measurements, and Cosmic Microwave Background (CMB) data.

- **Cosmic Chronometers (CC):**

  We use 15 measurements of the Hubble parameter obtained from the Cosmic Chronometers (CC) approach [48–53], which provide direct observational estimates of $H(z)$ over the redshift range $0 < z < 2$. For the CC data, we account for the full covariance between the measurements. Defining the residual vector as

$$\mathbf{r}_{\rm CC} = \mathbf{H}_{\rm obs} - \mathbf{H}_{\rm th}, \tag{40}$$

  where $\mathbf{H}_{\rm obs}$ and $\mathbf{H}_{\rm th}$ denote the vectors of observed and theoretically predicted Hubble parameters, respectively. The corresponding chi-square is given by

$$\chi^2_{\rm CC} = \mathbf{r}^T_{\rm CC}\mathbf{C}^{-1}_{\rm CC}\mathbf{r}_{\rm CC}, \tag{41}$$

  where $\mathbf{C}_{\rm CC}$ is the full 15×15 covariance matrix of the CC measurements.

- **Pantheon$^+$ Supernovae (PP):**

  We incorporate the Pantheon$^+$ Type Ia supernova compilation, consisting of 1588 SNIa data points together with the full statistical and systematic covariance matrix [4]. To minimize the impact of peculiar-velocity effects at very low redshifts, we adopt a redshift cut of $z > 0.01$. We use the uncalibrated Pantheon$^+$ sample, without imposing an external SH0ES prior on the Hubble constant H_0.

  The Pantheon$^+$ compilation provides the observed distance modulus $\mu_{\rm obs}(z_i)$. The theoretical distance modulus is given by

$$\mu_{\rm th}(z) = 5\log_{10}\left[\frac{D_L(z)}{\rm Mpc}\right] + 25, \tag{42}$$

  where $D_L(z)$ is the luminosity distance. For a spatially curved background, the luminosity distance is related to the transverse comoving distance by

$$D_L(z) = (1+z)D_M(z), \tag{43}$$

  where

$$D_M(z) = \begin{cases} \dfrac{c}{H_0\sqrt{\Omega_k}}\sinh\left[\sqrt{\Omega_k}\displaystyle\int_0^z \frac{dz'}{E(z')}\right], & \Omega_k > 0, \\ \dfrac{c}{H_0}\displaystyle\int_0^z \frac{dz'}{E(z')}, & \Omega_k = 0, \\ \dfrac{c}{H_0\sqrt{-\Omega_k}}\sin\left[\sqrt{-\Omega_k}\displaystyle\int_0^z \frac{dz'}{E(z')}\right], & \Omega_k < 0. \end{cases} \tag{44}$$

  Here,

$$E(z) = \frac{H(z)}{H_0} \tag{45}$$

  denotes the normalized Hubble parameter.

The absolute-magnitude (equivalently, Hubble-intercept) nuisance parameter is analytically marginalized. Defining the residual vector

$$\Delta\boldsymbol{\mu} = \boldsymbol{\mu}_{\rm obs} - \boldsymbol{\mu}_{\rm th}, \tag{46}$$

the marginalized chi-square is

$$\chi^2_{\rm SN} = \Delta\boldsymbol{\mu}^T C_{\rm SN}^{-1} \Delta\boldsymbol{\mu} - \frac{\left(\mathbf{1}^T C_{\rm SN}^{-1}\Delta\boldsymbol{\mu}\right)^2}{\mathbf{1}^T C_{\rm SN}^{-1}\mathbf{1}}, \tag{47}$$

where $\mathbf{1}$ denotes a vector of ones with the same dimension as the Pantheon$^+$ data vector.

- **DESI DR2 BAO:**

  We use the DESI DR2 BAO measurements, comprising 13 measurements at the redshifts $z = \{0.295, 0.510, 0.706, 0.934, 1.321, 1.484, 2.33\}$, with the corresponding BAO observables D_V/r_d, D_M/r_d, and D_H/r_d [54, 55]. Here, r_d denotes the sound horizon at the drag epoch, for which we adopt the fiducial value $r_d = 147.05$ Mpc.

  The radial BAO distance measure is defined as

$$D_H(z) = \frac{c}{H(z)} = \frac{c}{H_0 E(z)}. \tag{48}$$

  The transverse comoving distance $D_M(z)$ accounts for the spatial curvature and is given in Eq. 44. The volume-averaged BAO distance used for the isotropic BAO measurements is

$$D_V(z) = \left[z\, D_M^2(z)\, D_H(z)\right]^{1/3}. \tag{49}$$

  For each redshift, the theoretical BAO observable is selected according to the corresponding measurement type:

$$\mathcal{O}_{\rm th}(z_i) = \begin{cases} D_V(z_i)/r_d, & \text{for } D_V/r_d, \\ D_M(z_i)/r_d, & \text{for } D_M/r_d, \\ D_H(z_i)/r_d, & \text{for } D_H/r_d. \end{cases} \tag{50}$$

  Defining the residual vector between the 13 observed and theoretical BAO measurements as

$$\boldsymbol{\Delta}_{\rm BAO} = \boldsymbol{\mathcal{O}}_{\rm obs} - \boldsymbol{\mathcal{O}}_{\rm th}, \tag{51}$$

  the BAO chi-square is evaluated using the full 13×13 covariance matrix,

$$\chi^2_{\rm BAO} = \boldsymbol{\Delta}^T_{\rm BAO} \mathbf{C}^{-1}_{\rm BAO} \boldsymbol{\Delta}_{\rm BAO}, \tag{52}$$

  where $\mathbf{C}_{\rm BAO}$ denotes the covariance matrix of the DESI DR2 BAO measurements. Thus, the correlations among the BAO measurements are fully included in the likelihood.

- **Cosmic Microwave Background Distance Priors (CMB):**

  To incorporate constraints from the early Universe, we use the compressed Planck 2018 CMB distance priors [9]. The CMB likelihood is constructed from the shift parameter R, the acoustic angular scale ℓ_A, and the physical baryon density $\omega_b h^2$. We adopt the recombination redshift $z_* = 1089.92$.

  The CMB shift parameter is defined as

$$R = \sqrt{\Omega_m}\, \frac{H_0 D_M(z_*)}{c}, \tag{53}$$

while the acoustic angular scale is given by

$$\ell_A = \pi \frac{D_M(z_*)}{r_d}, \tag{54}$$

where r_d is the sound horizon at the drag epoch and $D_M(z_*)$ calculated from the Eq. 44 for the spatial curvature. The observed CMB distance-prior vector adopted in our analysis is therefore

$$\mathbf{Y}_{\rm obs} = \left(R_{\rm obs}, \ell_{A,\rm obs}, (\omega_b h^2)_{\rm obs}\right), \tag{55}$$

with

$$R_{\rm obs} = 1.750235, \qquad \ell_{A,\rm obs} = 301.4707, \qquad (\omega_b h^2)_{\rm obs} = 0.02235976. \tag{56}$$

The residual vector is defined as

$$\Delta\mathbf{Y} = \mathbf{Y}_{\rm th} - \mathbf{Y}_{\rm obs}, \tag{57}$$

where

$$\mathbf{Y}_{\rm th} = \left(R_{\rm th}, \ell_{A,\rm th}, (\omega_b h^2)_{\rm th}\right). \tag{58}$$

We account for the correlations among the three CMB distance priors using the full 3×3 covariance matrix. The CMB chi-square is consequently evaluated as

$$\chi^2_{\rm CMB} = \Delta\mathbf{Y}^T \mathbf{C}^{-1}_{\rm CMB} \Delta\mathbf{Y}, \tag{59}$$

where the inverse covariance matrix used in the analysis is

$$\mathbf{C}^{-1}_{\rm CMB} = \begin{pmatrix} 94392.3971 & -1360.4913 & 1664517.2916 \\ -1360.4913 & 161.4349 & 3671.6180 \\ 1664517.2916 & 3671.6180 & 79719182.5162 \end{pmatrix}. \tag{60}$$

B. Methodology

To constrain the model parameters, we employ the Markov Chain Monte Carlo (MCMC) technique using the `emcee` Python library [56] within the Python 3 (*ipykernel*) environment. The analysis is performed using three different combinations of observational datasets: **(i.)** D_1 : PP + CC **(ii.)** D_2 : PP + CC + DESI DR2 **(iii.)** D_3 : PP + CC + DESI DR2 + CMB both in curved and flat geometry. In addition, ΛCDM models are constrained using the same combined datasets in order to provide a direct comparison with the spinor field dark energy models.

The total likelihood function is expressed as

$$\mathcal{L} = \mathcal{L}_{\rm CC}\, \mathcal{L}_{\rm SN}\, \mathcal{L}_{\rm BAO}\, \mathcal{L}_{\rm CMB}. \tag{61}$$

Accordingly, the full log-likelihood used in the MCMC analysis is given by

$$\ln \mathcal{L} = -\frac{1}{2}\left(\chi^2_{\rm CC} + \chi^2_{\rm SN} + \chi^2_{\rm BAO} + \chi^2_{\rm CMB}\right). \tag{62}$$

For the curved geometry, the parameter spaces explored for different models are

$$\begin{aligned} \Theta_{\rm GCG} &= \{A, \alpha, \Omega_{k0}, H_0\}, \\ \Theta_{\rm MCG} &= \{A, \alpha, W, \Omega_{k0}, H_0\}, \\ \Theta_{\rm wSFDE} &= \{W, \Omega_{k0}, \Omega_{m0}, H_0\}, \\ \Theta_{\Lambda\rm CDM} &= \{\Omega_{k0}, \Omega_{m0}, H_0\}. \end{aligned}$$

For the flat geometry, we set $\Omega_{k0} = 0$. The priors adopted in the present analysis are

$$\begin{aligned} 0 < A < 5, \qquad 0 < \alpha < 2, \qquad -1.5 < W < 0, \\ -0.2 < \Omega_{k0} < 0.2, \qquad 0 < \Omega_{m0} < 1, \qquad 50 < H_0 < 90. \end{aligned}$$

The χ^2 statistic is commonly used for cosmological parameter estimation, a direct comparison of different models based solely on $\chi^2_{\rm min}$ is not appropriate because the models contain different numbers of free parameters. In general, models with more free parameters tend to produce lower values of $\chi^2_{\rm min}$. Therefore, in this work we additionally employ model selection criteria, namely the Akaike Information Criterion (AIC) and the Bayesian Information Criterion (BIC), to compare the viability of different dark energy models. The total χ^2 for a combined observational dataset is defined as

$$\chi^2 = \sum_{\rm data} \chi^2_{\rm data}. \tag{63}$$

For the full combined datasets consisting of Cosmic Chronometers (CC), Pantheon$^+$ Type Ia Supernovae (PP), Baryon Acoustic Oscillation (BAO), and Cosmic Microwave Background (CMB) observations, one has

$$\chi^2 = \chi^2_{\rm CC} + \chi^2_{\rm SN} + \chi^2_{\rm BAO} + \chi^2_{\rm CMB}. \tag{64}$$

The reduced chi-square statistic is defined by

$$\chi^2_\nu = \frac{\chi^2_{\rm min}}{\rm dof}, \qquad {\rm dof} = N - k, \tag{65}$$

where k denotes the number of free parameters and N represents the total number of observational data points. A value of $\chi^2_\nu \approx 1$ indicates a good fit between the model and observational data.

Table 1: Constraints on cosmological parameters for different models in curved geometry ($\Omega_k \neq 0$) using datasets D_1, D_2, and D_3.

Dataset	Model	A	α	W	Ω_{k0}	Ω_{m0}	H_0
D_1	GCG	$2.4047^{+0.5408}_{-0.3813}$	$0.1789^{+0.2543}_{-0.1307}$	–	$0.1313^{+0.0513}_{-0.1075}$	–	$66.56^{+3.93}_{-3.88}$
	MCG	$1.0434^{+0.9144}_{-0.5176}$	$0.6590^{+0.8082}_{-0.4976}$	$-0.2266^{+0.1421}_{-0.1086}$	$0.0856^{+0.0855}_{-0.1539}$	–	$67.14^{+3.93}_{-3.98}$
	wSFDE	–	–	$-0.8303^{+0.1226}_{-0.1594}$	$0.0131^{+0.1288}_{-0.1443}$	$0.2661^{+0.0718}_{-0.0738}$	$67.06^{+3.86}_{-3.87}$
	ΛCDM	–	–	–	$0.074^{+0.090}_{-0.138}$	$0.309^{+0.074}_{-0.049}$	$66.73^{+3.90}_{-3.87}$
D_2	GCG	$2.3309^{+0.1373}_{-0.1190}$	$0.0319^{+0.0349}_{-0.0225}$	–	$0.1415^{+0.0372}_{-0.0457}$	–	$67.79^{+0.55}_{-0.53}$
	MCG	$1.7689^{+0.3607}_{-0.2918}$	$0.1024^{+0.1573}_{-0.0761}$	$-0.0613^{+0.0337}_{-0.0339}$	$0.0296^{+0.0503}_{-0.0503}$	–	$67.82^{+0.60}_{-0.60}$
	wSFDE	–	–	$-0.8793^{+0.0494}_{-0.0548}$	$-0.0034^{+0.0489}_{-0.0493}$	$0.2982^{+0.0120}_{-0.0122}$	$67.35^{+0.61}_{-0.60}$
	ΛCDM	–	–	–	$0.068^{+0.034}_{-0.034}$	$0.290^{+0.012}_{-0.012}$	$68.17^{+0.48}_{-0.48}$
D_3	GCG	$2.4290^{+0.0426}_{-0.0422}$	$0.0411^{+0.0190}_{-0.0180}$	–	$0.0092^{+0.0037}_{-0.0036}$	–	$68.88^{+0.40}_{-0.40}$
	MCG	$2.5164^{+0.0652}_{-0.0513}$	$0.0060^{+0.0099}_{-0.0045}$	$-0.00075^{+0.00056}_{-0.00117}$	$0.00022^{+0.00143}_{-0.00195}$	–	$69.58^{+0.37}_{-0.35}$
	wSFDE	–	–	$-0.9136^{+0.0231}_{-0.0231}$	$0.0044^{+0.0011}_{-0.0012}$	$0.3032^{+0.0052}_{-0.0052}$	$67.52^{+0.58}_{-0.56}$
	ΛCDM	–	–	–	$0.002^{+0.001}_{-0.001}$	$0.288^{+0.003}_{-0.003}$	$69.37^{+0.33}_{-0.33}$

The Akaike and Bayesian information criteria are respectively defined as

$$\mathrm{AIC} = \chi^2_{\rm min} + 2k, \tag{66a}$$

$$\mathrm{BIC} = \chi^2_{\rm min} + k \ln N. \tag{66b}$$

A model with a smaller AIC value is generally more favored by observational data. Among several competing models, the model with the minimum AIC value is taken as the reference model. The relative difference is then defined as

$$\Delta\mathrm{AIC} = \mathrm{AIC}_{\rm model} - \mathrm{AIC}_{\rm ref}.$$

Typically, $0 < \Delta\mathrm{AIC} < 2$ indicates substantial support for the model, $4 < \Delta\mathrm{AIC} < 7$ suggests considerably less support, while $\Delta\mathrm{AIC} > 10$ implies essentially no support relative to the reference model. Similarly, for the Bayesian Information Criterion,

$$\Delta\mathrm{BIC} = \mathrm{BIC}_{\rm model} - \mathrm{BIC}_{\rm ref}.$$

A difference of $\Delta\text{BIC} > 2$ is regarded as positive evidence against the model with the larger BIC value, whereas $\Delta\text{BIC} > 6$ is considered strong evidence against that model. Although Bayesian evidence provides a more rigorous framework for model selection, the AIC and BIC criteria offer computationally efficient and widely used approximations for comparing cosmological models with different parameter spaces.

For the MCMC simulations, we fix the remaining model constants to $\lambda_1 = 1.0$ and $\lambda = 1.0$. The sound horizon scale is taken as $r_d = 147.05\,\text{Mpc}$, consistent with standard BAO analyses. In the numerical implementation, we employ 48 walkers with 3000 steps for each Markov chain.

IV. Results and Discussion

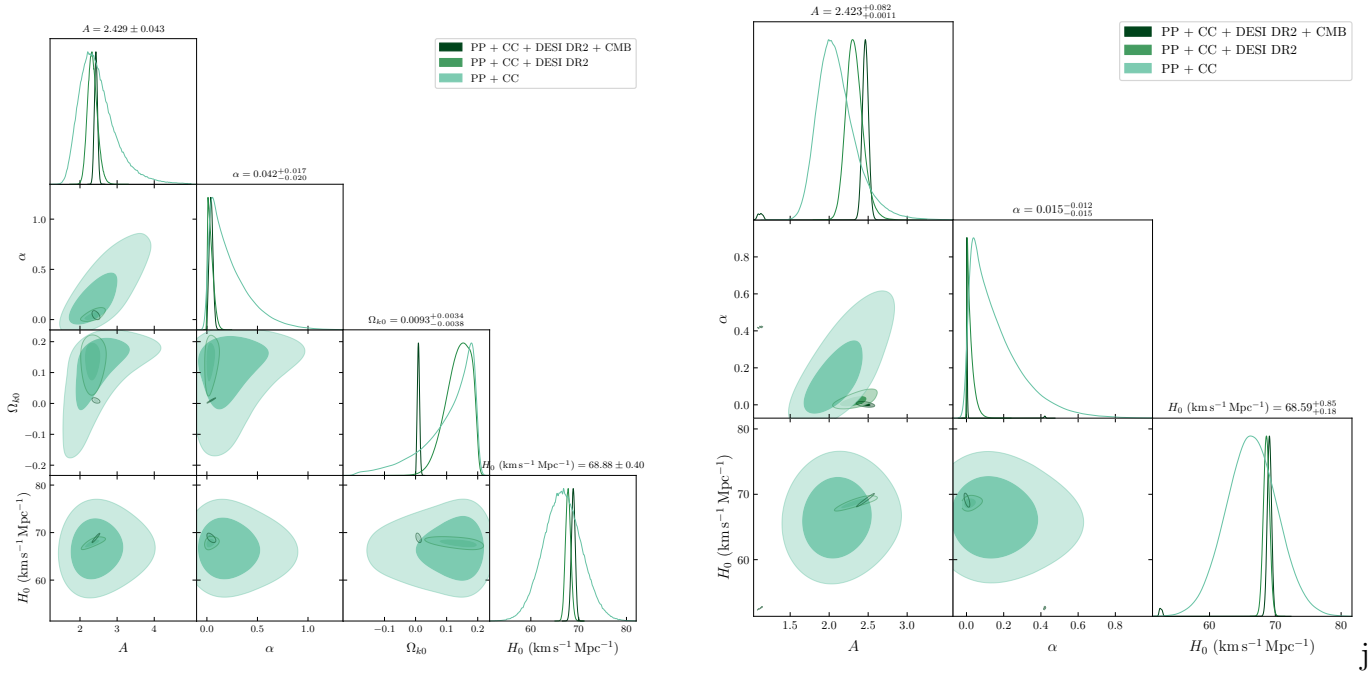
To perform a comparative observational study of the nonlinear spinor field generalized Chaplygin gas (GCG), modified Chaplygin gas (MCG), wSFDE, and ΛCDM models, we constrain the cosmological parameters using three combined observational datasets: **(i.)** D_1 : PP + CC, **(ii.)** D_2 : PP + CC + DESI DR2, and **(iii.)** D_3 : PP + CC + DESI DR2 + CMB, in both curved and flat geometries. The corresponding MCMC constraints at the 1σ confidence level are presented in Table 1 for curved geometry and in Table 2 for flat geometry using the D_1, D_2, and D_3 data combinations.

Table 2: Constraints on cosmological parameters for different models in flat geometry using datasets D_1, D_2, and D_3.

Dataset	Model	A	α	W	Ω_{k0}	Ω_{m0}	H_0
D_1	GCG	$2.072^{+0.270}_{-0.203}$	$0.126^{+0.177}_{-0.093}$	–	0 (fixed)	–	$66.40^{+3.88}_{-3.87}$
	MCG	$0.883^{+0.597}_{-0.405}$	$0.663^{+0.799}_{-0.499}$	$-0.242^{+0.125}_{-0.097}$	0 (fixed)	–	$67.10^{+3.93}_{-3.91}$
	wSFDE	–	–	$-0.829^{+0.118}_{-0.137}$	0 (fixed)	$0.274^{+0.063}_{-0.071}$	$66.92^{+3.94}_{-3.93}$
	ΛCDM	–	–	–	0 (fixed)	$0.350^{+0.020}_{-0.020}$	$66.58^{+3.88}_{-3.88}$
D_2	GCG	$2.319^{+0.115}_{-0.098}$	$0.016^{+0.024}_{-0.012}$	–	0 (fixed)	–	$68.65^{+0.47}_{-0.46}$
	MCG	$1.651^{+0.233}_{-0.210}$	$0.099^{+0.154}_{-0.074}$	$-0.070^{+0.026}_{-0.030}$	0 (fixed)	–	$67.75^{+0.58}_{-0.57}$
	wSFDE	–	–	$-0.883^{+0.040}_{-0.040}$	0 (fixed)	$0.298^{+0.009}_{-0.009}$	$67.38^{+0.59}_{-0.58}$
	ΛCDM	–	–	–	0 (fixed)	$0.310^{+0.010}_{-0.010}$	$68.52^{+0.45}_{-0.45}$
D_3	GCG	$2.463^{+0.040}_{-0.042}$	$0.002^{+0.003}_{-0.001}$	–	0 (fixed)	–	$69.09^{+0.33}_{-0.35}$
	MCG	$2.515^{+0.063}_{-0.050}$	$0.006^{+0.010}_{-0.005}$	$-0.0008^{+0.0005}_{-0.0006}$	0 (fixed)	–	$69.52^{+0.35}_{-0.34}$
	wSFDE	–	–	$-0.937^{+0.021}_{-0.021}$	0 (fixed)	$0.299^{+0.005}_{-0.005}$	$67.65^{+0.55}_{-0.54}$
	ΛCDM	–	–	–	0 (fixed)	$0.289^{+0.003}_{-0.003}$	$69.01^{+0.31}_{-0.31}$

From Tables 1 and 2, it is evident that the inclusion of the DESI DR2 BAO and CMB distance-prior data substantially tightens the cosmological constraints for all the considered models. This improvement is particularly pronounced when moving from D_1 to D_2 and subsequently to D_3, reflecting the complementary constraining power of the low-redshift and early-Universe observations. For the D_3 dataset, the GCG parameter α is strongly driven toward small values, with $\alpha = 0.0411^{+0.0190}_{-0.0180}$ in curved geometry and $\alpha = 0.002^{+0.003}_{-0.001}$ in flat geometry, indicating a strong tendency toward the ΛCDM limit. Similarly, the MCG parameter α becomes very small for D_3, while the parameter W is constrained to be very close to zero, $W = -0.00075^{+0.00056}_{-0.00117}$ and $W = -0.0008^{+0.0005}_{-0.0006}$ for curved and flat geometries, respectively. Thus, the D_3 combination strongly restricts the additional degrees of freedom in the Chaplygin-gas models.

The curvature constraints also become considerably tighter with the addition of DESI DR2 and CMB data. For D_3, the GCG model gives $\Omega_{k0} = 0.0092^{+0.0037}_{-0.0036}$, while the MCG and ΛCDM models yield $\Omega_{k0} = 0.00022^{+0.00143}_{-0.00195}$ and $\Omega_{k0} = 0.002^{+0.001}_{-0.001}$, respectively. The wSFDE model gives a slightly larger but still small curvature, $\Omega_{k0} = 0.0044^{+0.0011}_{-0.0012}$. These results indicate that the combined D_3 dataset strongly favours a geometry very close to spatial flatness. The corresponding flat-geometry



(a) Curved geometry ($\Omega_k \neq 0$).

(b) Flat geometry ($\Omega_k = 0$).

Figure 1: Marginalized 1σ confidence contours for the spinor-field generalized Chaplygin gas (GCG) model using the combined datasets D_1, D_2, and D_3.

constraints are consistent with this behaviour, with the matter density for wSFDE and ΛCDM constrained to $\Omega_{m0} = 0.299 \pm 0.005$ and $\Omega_{m0} = 0.289 \pm 0.003$, respectively. The inferred Hubble constant also becomes substantially tighter for D_3, with values ranging from approximately 67.5 $\mathrm{km\,s^{-1}\,Mpc^{-1}}$ for wSFDE to 69.6 $\mathrm{km\,s^{-1}\,Mpc^{-1}}$ for the MCG model. The corresponding confidence contour plots are displayed in Figs. 1–4, where panel (a) corresponds to curved geometry ($\Omega_k \neq 0$) and panel (b) represents flat geometry ($\Omega_k = 0$).

Table 3: Present-day equation of state parameter w_0, deceleration parameter q_0, and transition redshift z_t for different dark energy models using the combined dataset D3. Results are shown for both curved and flat geometries.

Dataset	Model	Curved Geometry			Flat Geometry		
		w_0	q_0	z_t	w_0	q_0	z_t
D_3	GCG	-0.709	-0.559	0.659	-0.711	-0.565	0.699
	MCG	-0.716	-0.573	0.711	-0.716	-0.571	0.709
	wSFDE	-0.912	-0.448	0.654	-0.938	-0.483	0.673
	ΛCDM	-1.000	-0.564	0.701	-1.000	-0.565	0.702

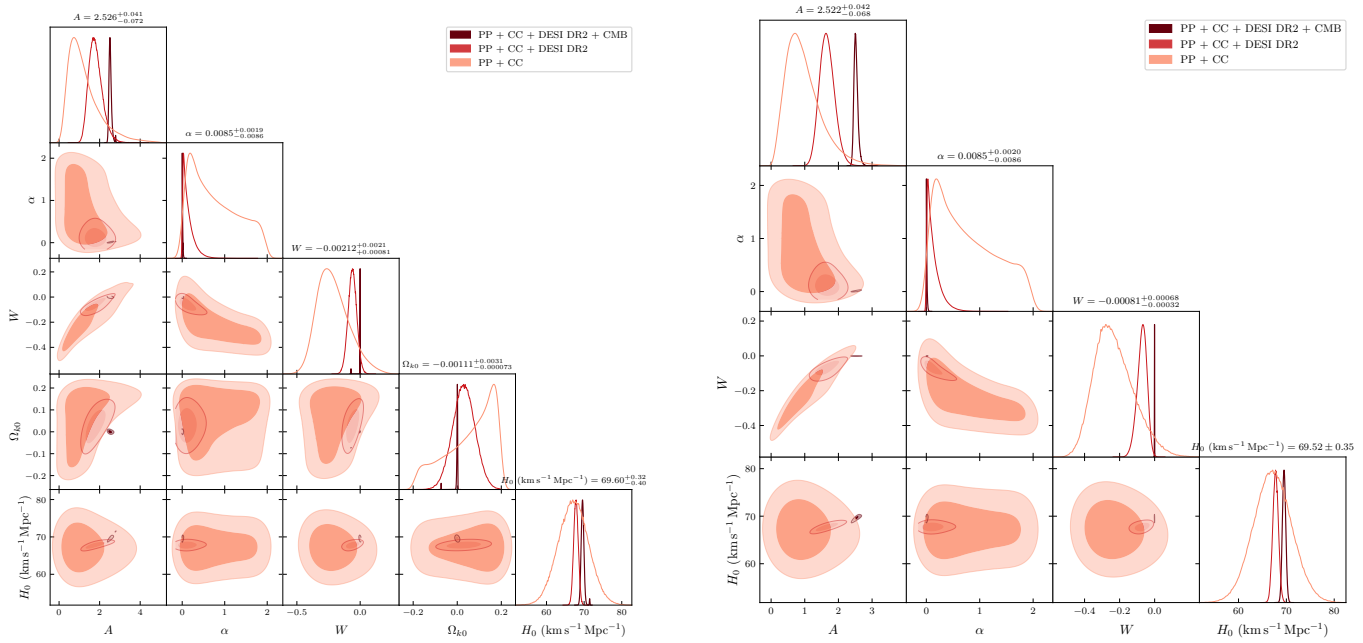
Figs. 5 and 6 illustrate the evolution of the equation of state parameter $w(z)$ and the deceleration parameter $q(z)$ for the GCG, MCG, wSFDE, and ΛCDM models using the combined dataset D_3. In both curved and flat geometries, all models exhibit the expected transition from a decelerated phase at higher redshift to an accelerated phase at late times, as indicated by the change of $q(z)$ from positive to negative values. The GCG and MCG models show a smooth evolution of the equation of state toward their present-day values, with the MCG model remaining close to $w_0 \simeq -0.72$ in both geometries. The GCG model also approaches ΛCDM-like behaviour at late times, consistent with the small value of α obtained from the D_3 constraints. The wSFDE model exhibits a more negative equation of state, particularly in flat geometry, where $w_0 \simeq -0.94$, while its curved-geometry value is $w_0 \simeq -0.91$. Nevertheless, the wSFDE model remains above the phantom boundary ($w = -1$) at the present epoch. The ΛCDM model, as expected, has a constant equation of state $w = -1$.

Table 4: Comparison of models using χ^2 statistics for curved and flat geometries. The curvature effect is quantified as $\Delta\chi^2_{\rm geo} = \chi^2_{\rm flat} - \chi^2_{\rm curved}$ for each model. Positive values indicate a preference for curved geometry, while negative values favor flat geometry.

Dataset	Model	Curved Geometry			Flat Geometry			$\Delta\chi^2_{\rm geo}$
		$\chi^2_{\rm min}$	$\Delta\chi^2_{\rm min}$	χ^2_ν	$\chi^2_{\rm min}$	$\Delta\chi^2_{\rm min}$	χ^2_ν	
D_1	GCG	1441.01	1.64	0.901	1442.24	2.89	0.901	1.24
	MCG	1440.12	0.75	0.901	1440.38	1.02	0.901	0.25
	wSFDE	**1439.37**	**0.00**	0.900	**1439.36**	**0.00**	0.900	-0.01
	ΛCDM	1440.95	0.98	0.900	1440.95	1.59	0.900	0.60
D_2	GCG	1450.84	2.09	0.904	1458.67	9.92	0.904	7.84
	MCG	1454.09	5.35	0.902	1453.42	4.67	0.902	-0.67
	wSFDE	**1448.75**	**0.00**	0.898	**1448.76**	**0.00**	0.898	0.01
	ΛCDM	1453.22	4.47	0.903	1457.29	8.53	0.903	4.07
D_3	GCG	1459.89	10.36	0.904	1468.23	3.11	0.909	8.34
	MCG	1466.91	17.38	0.909	1467.88	2.76	0.909	0.98
	wSFDE	**1449.53**	**0.00**	0.898	**1465.13**	**0.00**	0.907	15.60
	ΛCDM	1464.20	14.67	0.906	1473.46	8.34	0.911	9.26

Table 5: Model comparison using the Akaike Information Criterion (AIC) and Bayesian Information Criterion (BIC) for different datasets and geometries. Typically, $\Delta < 2$ indicates substantial support, $4 < \Delta < 7$ indicates considerably less support, and $\Delta > 10$ indicates strong evidence against the model.

Dataset	Model	Curved Geometry				Flat Geometry			
		AIC	ΔAIC	BIC	ΔBIC	AIC	ΔAIC	BIC	ΔBIC
D_1	GCG	1449.01	2.66	1470.53	8.04	1448.24	3.29	1464.38	8.67
	MCG	1450.12	3.77	1477.02	14.53	1448.38	3.43	1469.90	14.19
	wSFDE	1447.37	1.02	1468.89	6.40	1445.36	0.41	1461.49	5.78
	ΛCDM	**1446.35**	**0.00**	**1462.49**	**0.00**	**1444.95**	**0.00**	**1455.71**	**0.00**
D_2	GCG	1458.84	2.09	1480.39	5.00	1464.67	9.92	1480.84	9.92
	MCG	1464.09	7.35	1491.03	15.65	1461.42	6.67	1482.97	12.05
	wSFDE	**1456.75**	**0.00**	1478.30	2.91	**1454.76**	**0.00**	**1470.92**	**0.00**
	ΛCDM	1459.22	2.47	**1475.38**	**0.00**	1461.29	6.53	1472.06	1.14
D_3	GCG	1467.89	10.36	1489.45	10.36	1474.23	3.11	1490.40	3.11
	MCG	1476.91	19.38	1503.85	24.77	1475.88	4.76	1497.44	10.15
	wSFDE	**1457.53**	**0.00**	**1479.09**	**0.00**	**1471.13**	**0.00**	**1487.29**	**0.00**
	ΛCDM	1470.20	12.67	1486.37	7.28	1477.46	6.34	1488.24	0.95



(a) Curved geometry ($\Omega_k \neq 0$). (b) Flat geometry ($\Omega_k = 0$).

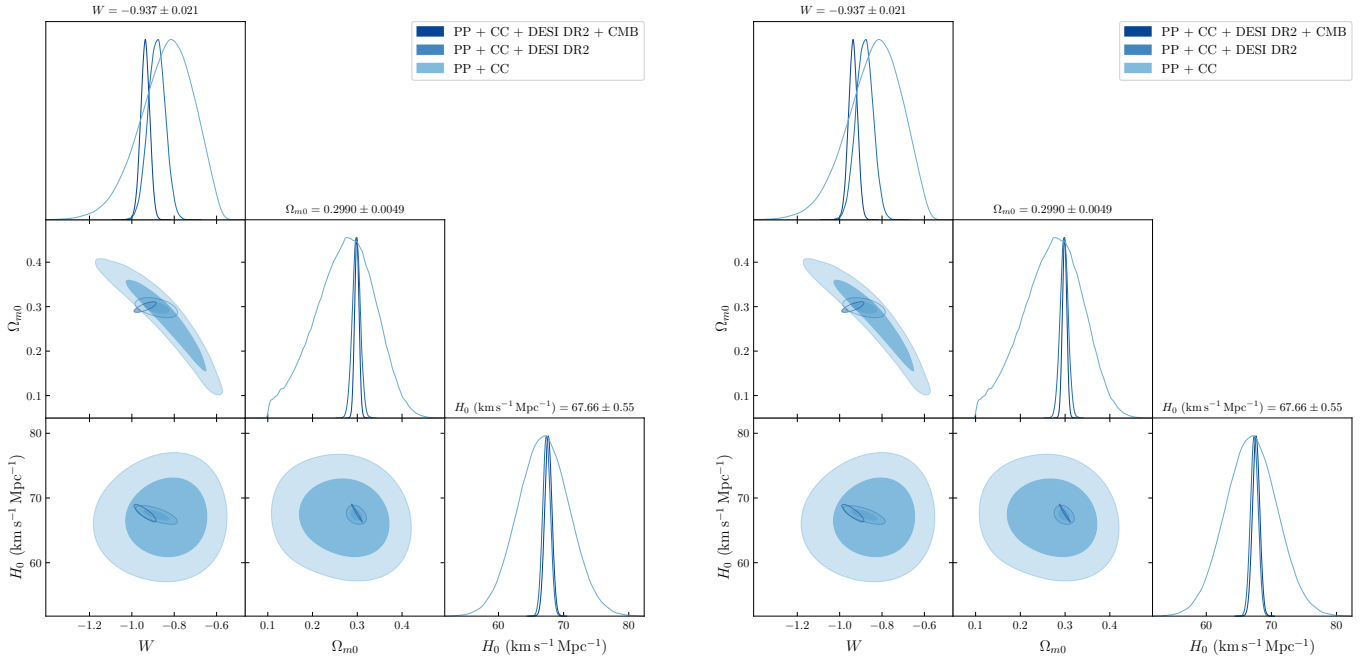
Figure 2: Marginalized 1σ confidence contours for the spinor-field modified Chaplygin gas (MCG) model using the combined datasets D_1, D_2, and D_3.

The corresponding present-day values of the equation of state parameter w_0, deceleration parameter q_0, and transition redshift z_t are summarized in Table 3. All models predict a presently accelerating Universe, with $q_0 < 0$ in both curved and flat geometries. The present-day deceleration parameter lies in the range $-0.573 \lesssim q_0 \lesssim -0.448$ for the curved models and $-0.565 \lesssim q_0 \lesssim -0.483$ for the flat models. The transition from deceleration to acceleration occurs at $z_t \simeq 0.65$–0.71, with the MCG and ΛCDM models giving the highest transition redshifts, while the wSFDE and curved GCG models yield slightly earlier transitions. The comparison of the present-day values of w_0 and q_0 for the four models is shown in the left and right panels, respectively, of Fig. 7.

The evolution of the Hubble parameter $H(z)$ and the corresponding residuals $\Delta H(z)$ for the combined dataset D_3 are presented in Fig. 8 and Fig. 9, respectively, for both curved and flat geometries. The predicted cosmological evolutions from the GCG, MCG, wSFDE, and ΛCDM models show good agreement with the observational CC data over the considered redshift range. Furthermore, Fig. 10 illustrates the evolution of the distance modulus $\mu(z)$, while the corresponding residuals $\Delta\mu(z) = \mu_{\rm obs} - \mu_{\rm model}$ are shown in Fig. 11 using the D_3 dataset. The residual distributions indicate that all the considered models provide an overall satisfactory fit to the observational supernova data, with comparatively smaller deviations in the flat geometry scenario.

From Table 4, we summarize the minimum chi-square values $\chi^2_{\rm min}$, reduced chi-square values χ^2_ν, and the relative chi-square differences $\Delta\chi^2_{\rm min} = \chi^2_{\rm model} - \chi^2_{\rm ref}$ for the considered cosmological models in both curved and flat geometries. For the D_1 dataset, the wSFDE model provides the lowest $\chi^2_{\rm min}$ in both curved and flat geometries, with $\chi^2_{\rm min} = 1439.37$ and 1439.36, respectively. A similar behaviour is obtained for D_2, for which wSFDE again gives the best fit, with $\chi^2_{\rm min} = 1448.75$ in curved geometry and 1448.76 in flat geometry. For the full D_3 dataset, the wSFDE model continues to provide the lowest minimum chi-square, yielding $\chi^2_{\rm min} = 1449.53$ for curved geometry and $\chi^2_{\rm min} = 1465.13$ for flat geometry. The reduced chi-square values remain close to unity for all models and datasets, indicating acceptable overall fits to the combined observations.

To quantify the effect of spatial curvature on the goodness of fit, we define the geometrical chi-square difference as $\Delta\chi^2_{\rm geo} = \chi^2_{\rm flat} - \chi^2_{\rm curved}$. Positive values therefore indicate a lower χ^2 for the curved geometry, whereas negative values favour the flat geometry. For D_1, the geometrical differences are relatively small for all models, with $\Delta\chi^2_{\rm geo} = 1.24$, 0.25, -0.01, and 0.60 for GCG, MCG, wSFDE, and ΛCDM, respectively. Similarly, for D_2, the curvature dependence remains modest



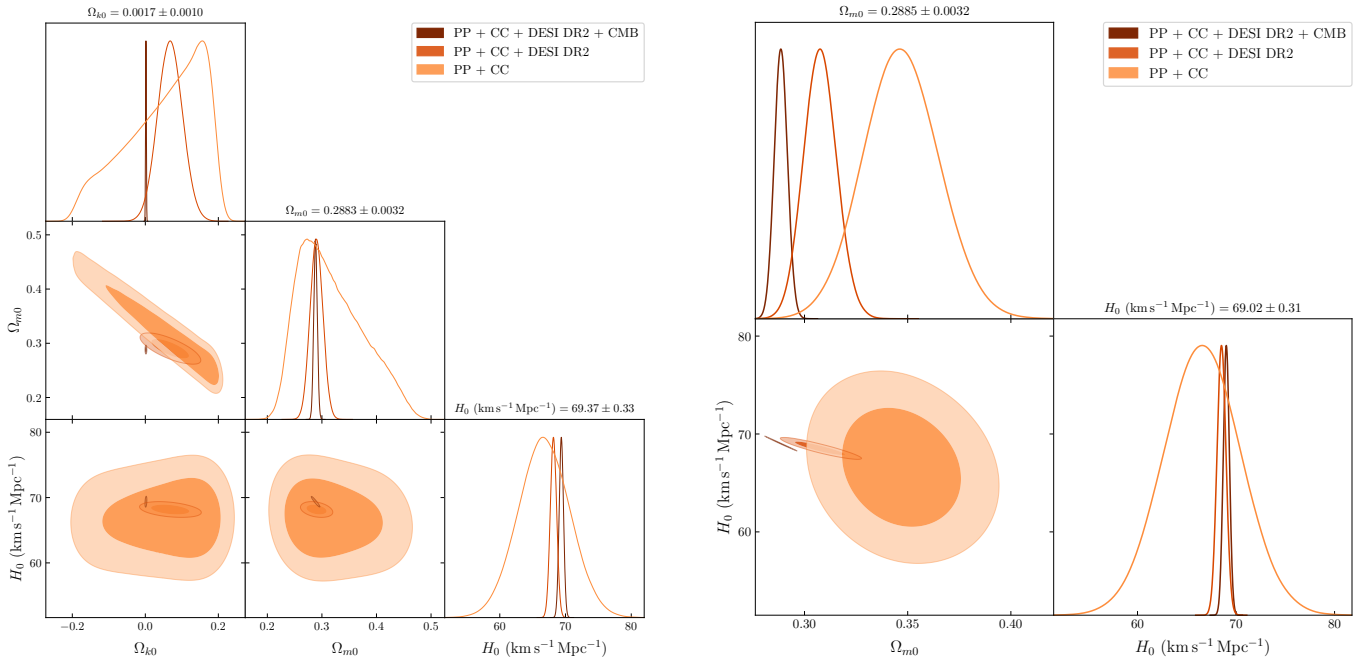
(a) Curved geometry ($\Omega_k \neq 0$). (b) Flat geometry ($\Omega_k = 0$).

Figure 3: Marginalized 1σ confidence contours for the spinor-field wSFDE model using the combined datasets D_1, D_2, and D_3.

for MCG and wSFDE, with $\Delta\chi^2_{\rm geo} = -0.67$ and 0.01, respectively, while GCG and ΛCDM show somewhat larger preferences for curved geometry, with $\Delta\chi^2_{\rm geo} = 7.84$ and 4.07. For the full D_3 dataset, the curvature dependence becomes more pronounced. The GCG model gives $\Delta\chi^2_{\rm geo} = 8.34$, while ΛCDM gives $\Delta\chi^2_{\rm geo} = 9.26$, both indicating a substantially better minimum χ^2 for curved geometry. The MCG model exhibits only a small difference, $\Delta\chi^2_{\rm geo} = 0.98$, indicating that its goodness of fit is relatively insensitive to the inclusion of spatial curvature. Most notably, the wSFDE model yields $\Delta\chi^2_{\rm geo} = 15.60$, corresponding to a substantially lower χ^2 in curved geometry than in the flat case. Therefore, for the D_3 dataset, the improvement associated with allowing spatial curvature is strongest for wSFDE, followed by ΛCDM and GCG, whereas MCG shows only a modest geometrical dependence. The comparative behaviour of $\Delta\chi^2_{\rm min}$ for the D_3 dataset is illustrated in Fig. 12.

Using the Akaike Information Criterion (AIC) and Bayesian Information Criterion (BIC), we further assess the relative statistical preference among the considered cosmological models. The corresponding ΔAIC and ΔBIC values are summarized in Table 5. For the D_1 dataset, ΛCDM provides the preferred model according to both AIC and BIC in curved and flat geometries, with $\Delta AIC = \Delta BIC = 0$ in each case. The wSFDE model remains comparatively competitive, with $\Delta AIC = 1.02$ and 0.41 for curved and flat geometries, respectively, while its ΔBIC values are 6.40 and 5.78. The GCG and MCG models receive weaker support, particularly according to the BIC, owing to their larger number of free parameters. For the D_2 dataset, the AIC favours the wSFDE model in both curved and flat geometries, with $\Delta AIC = 0$. In curved geometry, the wSFDE model also has a relatively small $\Delta BIC = 2.91$, whereas ΛCDM has the minimum BIC with $\Delta BIC = 0$. In flat geometry, wSFDE is preferred by AIC, while ΛCDM remains competitive according to BIC, with $\Delta BIC = 1.14$. Thus, the information criteria give somewhat different rankings for D_2, reflecting the stronger penalty imposed by BIC on models with additional parameters.

The inclusion of the CMB information in the D_3 dataset leads to a clearer model preference. In curved geometry, the wSFDE model is strongly favoured by both information criteria, with $\Delta AIC = 0$ and $\Delta BIC = 0$. The GCG model has $\Delta AIC = 10.36$ and $\Delta BIC = 10.36$, while MCG is strongly disfavoured with $\Delta AIC = 19.38$ and $\Delta BIC = 24.77$. ΛCDM also receives substantially weaker support than wSFDE, with $\Delta AIC = 12.67$ and $\Delta BIC = 7.28$. In flat geometry, wSFDE again gives the minimum AIC, with $\Delta AIC = 0$, while ΛCDM is highly competitive according to BIC, with



(a) Curved geometry ($\Omega_k \neq 0$). (b) Flat geometry ($\Omega_k = 0$).

Figure 4: Marginalized 1σ confidence contours for the ΛCDM model using the combined datasets D_1, D_2, and D_3.

$\Delta BIC = 0$. The corresponding ΔAIC values are 3.11, 4.76, and 6.34 for GCG, MCG, and ΛCDM, respectively. According to BIC, MCG is substantially disfavoured ($\Delta BIC = 10.15$), whereas GCG and ΛCDM remain within $\Delta BIC < 10$. The comparative behaviour of the information criteria for the D_3 dataset is illustrated in Fig. 13, where the left and right panels show the corresponding ΔAIC and ΔBIC values, respectively.

Considering the minimum χ^2 values together with the AIC and BIC statistics, the wSFDE model provides the strongest overall statistical performance for the combined D_3 dataset. In curved geometry, wSFDE is consistently preferred by all three criteria, yielding the lowest $\chi^2_{\rm min} = 1449.53$, $\Delta AIC = 0$, and $\Delta BIC = 0$. Moreover, the curved wSFDE model is strongly preferred over its flat counterpart, with a geometrical difference of $\Delta\chi^2_{\rm geo} = 15.60$. In flat geometry, wSFDE remains the preferred model according to AIC, while ΛCDM is preferred by BIC. Therefore, when the goodness of fit and both information criteria are considered jointly, the curved wSFDE model emerges as the most consistently supported model for the full D_3 dataset.

For completeness, we further examine the parameter constraints of the curved wSFDE model for the full D_3 dataset, which provides the statistically preferred description according to the combined χ^2, AIC, and BIC analyses. The model yields $W = -0.9136^{+0.0231}_{-0.0231}$, together with a small but non-zero curvature parameter $\Omega_{k0} = 0.0044^{+0.0011}_{-0.0012}$ and a matter density $\Omega_{m0} = 0.3032^{+0.0052}_{-0.0052}$. The present-day Hubble constant is constrained to $H_0 = 67.52^{+0.58}_{-0.56}\ \mathrm{km\,s^{-1}\,Mpc^{-1}}$. The small value of Ω_{k0} indicates that the preferred curved wSFDE model remains very close to spatial flatness, while the value of W is consistent with a dark-energy-dominated accelerated expansion. These constraints, together with the significantly lower $\chi^2_{\rm min}$ and the minimum AIC and BIC values, make the curved wSFDE model the most statistically favoured scenario for the combined D_3 dataset among the models considered.

V. Conclusion

In this work, we have performed a comprehensive comparative analysis of the spinor-field-inspired generalized Chaplygin gas (GCG), modified Chaplygin gas (MCG), wSFDE, and standard ΛCDM cosmological models. The cosmological parameters of these models were constrained using a Markov Chain Monte Carlo (MCMC) analysis with several recent observational datasets, namely Cosmic

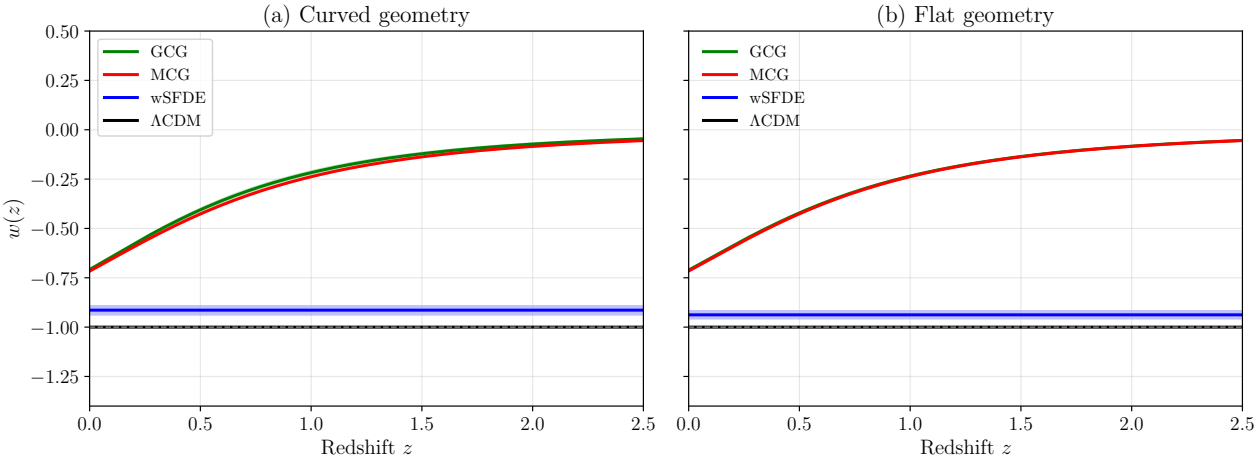


Figure 5: Evolution of the equation of state parameter $w(z)$ for different cosmological models using the combined dataset D_3 (PP + CC + DESI DR2 + CMB). The left panel (a) corresponds to the curved geometry ($\Omega_k \neq 0$), while the right panel (b) represents the flat geometry ($\Omega_k = 0$). The shaded regions denote the 1σ confidence intervals obtained from the MCMC analysis. The horizontal dashed line at $w = -1$ indicates the ΛCDM limit.

Chronometers (CC), Pantheon$^+$ Type Ia supernovae (PP), DESI DR2 baryon acoustic oscillation (BAO) measurements, and Planck CMB distance priors. The analysis was performed for three combined datasets, namely D_1: PP + CC, D_2: PP + CC + DESI DR2, and D_3: PP + CC + DESI DR2 + CMB, considering both curved ($\Omega_k \neq 0$) and spatially flat ($\Omega_k = 0$) geometries.

The observational constraints demonstrate that all four considered models provide viable descriptions of the late-time expansion history of the Universe. The addition of DESI DR2 BAO and CMB information substantially improves the precision of the cosmological parameters, particularly for the full D_3 dataset. For the D_3 combination, the curvature constraints become very tight, with $\Omega_{k0} = 0.0092^{+0.0037}_{-0.0036}$ for GCG, $\Omega_{k0} = 0.00022^{+0.00143}_{-0.00195}$ for MCG, $\Omega_{k0} = 0.0044^{+0.0011}_{-0.0012}$ for wSFDE, and $\Omega_{k0} = 0.002 \pm 0.001$ for ΛCDM. Thus, all the curved models remain very close to spatial flatness when the full D_3 dataset is considered. In particular, the curved wSFDE model, despite providing the statistically preferred fit, requires only a small positive curvature.

The constraints on the dark-energy parameters also reveal an interesting convergence toward ΛCDM-like behaviour for the Chaplygin-gas models. For the D_3 dataset, the GCG parameter α is constrained to $0.0411^{+0.0190}_{-0.0180}$ in curved geometry and $0.002^{+0.003}_{-0.001}$ in flat geometry. Similarly, the MCG model gives $\alpha = 0.0060^{+0.0099}_{-0.0045}$ and $W = -0.00075^{+0.00056}_{-0.00117}$ in curved geometry, with comparable values in flat geometry. These small values indicate that the additional Chaplygin-gas degrees of freedom are strongly restricted by the combined D_3 observations. The wSFDE model, on the other hand, gives $W = -0.9136 \pm 0.0231$ in curved geometry and $W = -0.937 \pm 0.021$ in flat geometry. Both values remain above the phantom boundary $w = -1$ at the present epoch.

The reconstructed evolution of the equation of state parameter $w(z)$ and the deceleration parameter $q(z)$ further demonstrates that all models reproduce the transition from an early decelerated phase to the present accelerated expansion of the Universe. The present-day values satisfy $q_0 < 0$ for all models and both geometries. The transition from deceleration to acceleration occurs at $z_t \simeq 0.65$–0.71, with the corresponding values summarized in Table 3. The MCG and ΛCDM models exhibit transition redshifts close to $z_t \simeq 0.70$, while the GCG and wSFDE models give slightly lower values. The present-day equation of state parameters also show that GCG and MCG have similar late-time behaviour, whereas wSFDE exhibits a more negative but still non-phantom equation of state. The Hubble parameter evolution, distance-modulus comparison, and residual distributions further demonstrate the consistency of the models with the CC and Pantheon$^+$ observations.

The statistical comparison provides a clear distinction among the models for the full D_3 dataset.

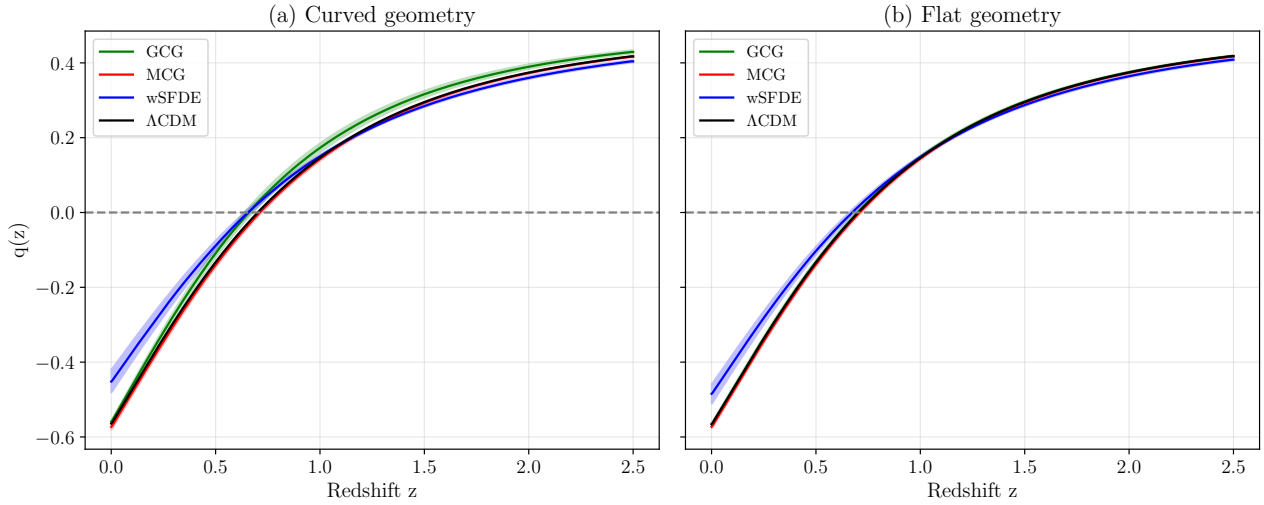


Figure 6: Evolution of the deceleration parameter $q(z)$ as a function of redshift z for different cosmological models, namely the generalized Chaplygin gas (GCG), modified Chaplygin gas (MCG), wSFDE, and ΛCDM. The left panel corresponds to the curved case ($\Omega_k \neq 0$), while the right panel represents the spatially flat case ($\Omega_k = 0$). The shaded regions denote the 1σ confidence intervals obtained from the MCMC analysis using the combined dataset (D3). The horizontal dashed line at $q = 0$ marks the transition from decelerated to accelerated expansion.

The minimum chi-square analysis shows that the curved wSFDE model gives the lowest value, $\chi^2_{\rm min} = 1449.53$, compared with 1459.89, 1466.91, and 1464.20 for curved GCG, MCG, and ΛCDM, respectively. Moreover, the curved wSFDE model has the minimum AIC and BIC values, with $\Delta\text{AIC} = \Delta\text{BIC} = 0$. The corresponding $\Delta\chi^2_{\rm geo} = 15.60$ indicates a substantial improvement in the minimum chi-square when spatial curvature is allowed for the wSFDE model. The GCG and ΛCDM models also show appreciable improvements upon allowing curvature, with $\Delta\chi^2_{\rm geo} = 8.34$ and 9.26, respectively, whereas the MCG model exhibits only a modest geometrical dependence, $\Delta\chi^2_{\rm geo} = 0.98$. These results indicate that the statistical preference for curvature is model dependent and is most pronounced for the wSFDE scenario. For the flat geometry, the information criteria also preferred the wSFDE according to AIC, BIC. However, the curved wSFDE model provides the most consistent statistical description of the full D_3 dataset. Its parameter constraints, $W = -0.9136 \pm 0.0231$, $\Omega_{k0} = 0.0044^{+0.0011}_{-0.0012}$, $\Omega_{m0} = 0.3032 \pm 0.0052$, and $H_0 = 67.52^{+0.58}_{-0.56}$ km s^{-1} Mpc^{-1}, remain physically viable and indicate a universe that is very close to spatial flatness while undergoing late-time accelerated expansion.

Overall, our analysis shows that the inclusion of DESI DR2 and CMB data provides substantially tighter constraints on the dark-energy models and reduces the allowed deviations from the standard cosmological behaviour. Although the GCG and MCG models approach ΛCDM-like behaviour for the full D_3 dataset, the statistical comparison favours the wSFDE scenario when spatial curvature is allowed to vary. The curved wSFDE model simultaneously provides the lowest $\chi^2_{\rm min}$ and the minimum AIC and BIC values for D_3, while requiring only a small positive curvature. Moreover, the wSFDE model is favored by both AIC and BIC in both the flat and curved geometries. Physically, the wSFDE model represents a more phenomenologically viable spinor-field dark-energy scenario than the unified GCG and MCG models, which face well-known difficulties, particularly concerning structure formation. In addition, the wSFDE model has fewer free parameters than the GCG and MCG models. Therefore, within the observational framework and model assumptions adopted in this work, the wSFDE model emerges as the most statistically favored and physically relevant scenario among the models considered.

Declarations:

Competing interests There is no conflict of interests.

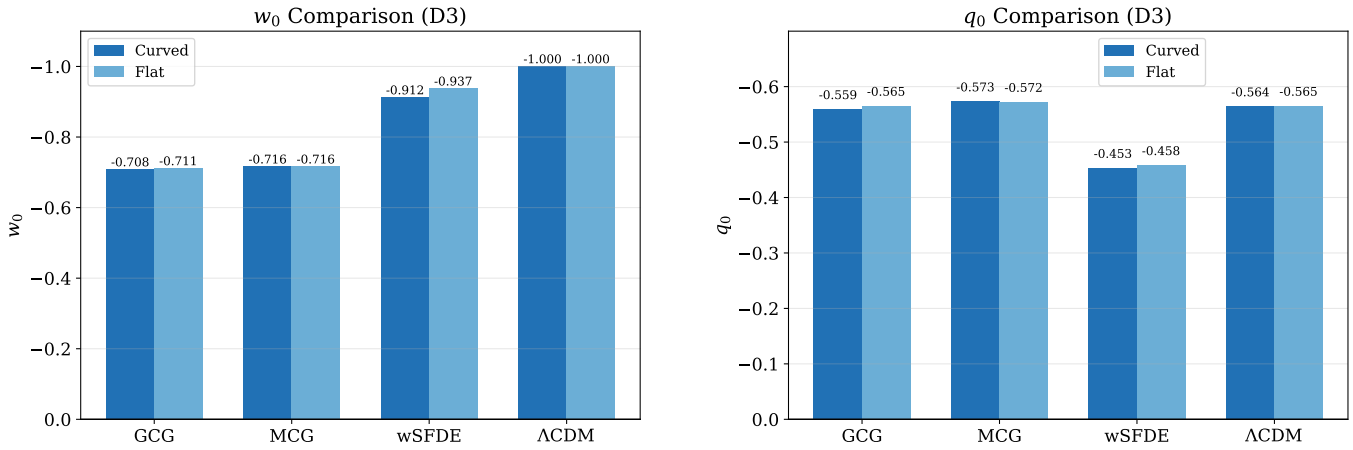


Figure 7: Comparison of the present-day equation of state parameter w_0 and deceleration parameter q_0 for the GCG, MCG, wSFDE, and ΛCDM models using the combined dataset D_3 (PP + CC + DESI DR2 + CMB). The left panel illustrates the corresponding values of w_0, while the right panel shows the present-day deceleration parameter q_0 for all considered cosmological models in both curved and flat geometries.

Funding Not applicable.

Availability of data and materials No new datasets were generated during the current study.

References

[1] A. G. Riess *et al.*, Astron. J. **116**, 1009 (1998), doi:10.1086/300499, arXiv:astro-ph/9805201.

[2] S. Perlmutter *et al.*, Astrophys. J. **517**, 565 (1999), doi:10.1086/307221, arXiv:astro-ph/9812133.

[3] D.M. Scolnic et al., Astrophys. J. **859**, 101 (2018), doi:10.3847/1538-4357/aab9bb, arXiv:1710.00845.

[4] D. Brout et al., Astrophys. J. **938**, 110 (2022), doi:10.3847/1538-4357/ac8e04, arXiv:2202.04077.

[5] S. Alam *et al.*, Phys. Rev. D **103**, 083533 (2021), doi:10.1103/PhysRevD.103.083533, arXiv:2007.08991.

[6] C.H. Hahn, *et al.*, Astrophys. J. **165**, 253 (2023), https://doi.org/10.3847/1538-3881/accff8, arXiv:2208.08512.

[7] DESI Collaboration: Astrophys. J. **168**, 58 (2024), https://doi.org/10.3847/1538-3881/ad3217, arXiv:2306.06308.

[8] Planck Collaboration, Astron. Astrophys. **571**, A16 (2014), doi:10.1051/0004-6361/201321591, arXiv:1303.5076.

[9] N. Aghanim *et al.* (Planck Collaboration), Astron. Astrophys. **641**, A6 (2020), doi:10.1051/0004-6361/201833910, arXiv:1807.06209.

[10] S. Weinberg, Rev. Mod. Phys. **61**, 1 (1989), doi:10.1103/RevModPhys.61.1.

[11] S. M. Carroll, Living Rev. Relativ. **4**, 1 (2001), doi:10.12942/lrr-2001-1, arXiv:astro-ph/0004075.

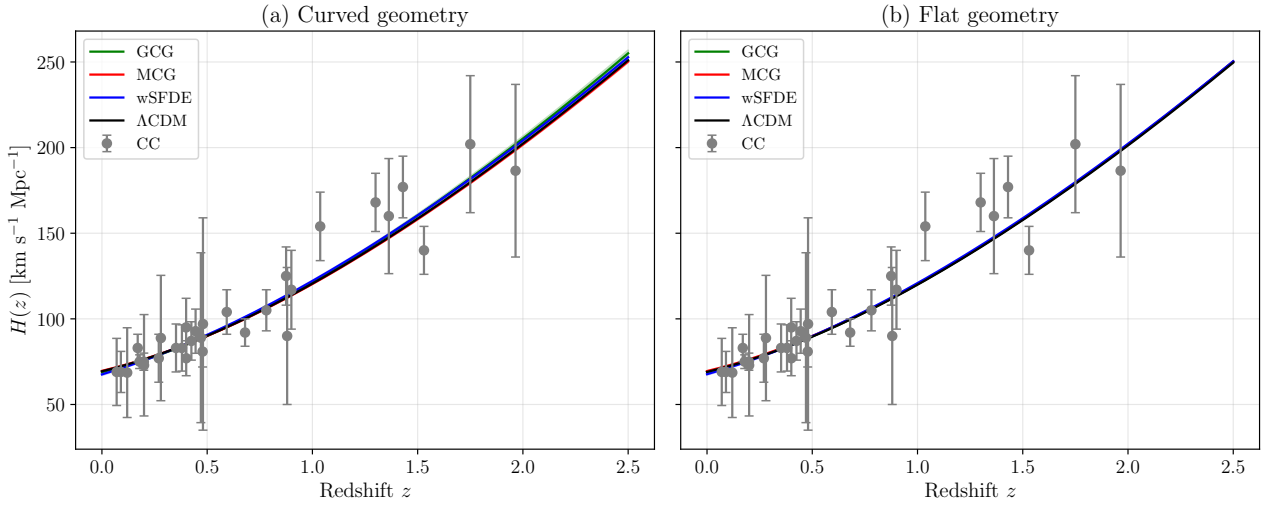


Figure 8: Evolution of the Hubble parameter $H(z)$ for different cosmological models using the combined dataset D_3. The left panel corresponds to curved geometry, while the right panel represents flat geometry. The shaded regions denote the 1σ confidence intervals obtained from the MCMC analysis, and the observational CC data points are shown for comparison.

[12] A. G. Riess *et al.*, Astrophys. J. **876**, 85 (2019), doi:10.3847/1538-4357/ab1422, arXiv:1903.07603.

[13] L. Verde, T. Treu and A. G. Riess, Nature Astron. **3**, 891 (2019), doi:10.1038/s41550-019-0902-0, arXiv:1907.10625.

[14] E. J. Copeland, M. Sami and S. Tsujikawa, Int. J. Mod. Phys. D **15**, 1753 (2006), doi:10.1142/S021827180600942X, arXiv:hep-th/0603057.

[15] DESI Collaboration et al.,(2025), https://doi.org/10.48550/arXiv.2503.14745.

[16] DESI Collaboration et al., Phys. Rev. D **112**, 083515 (2025), https://doi.org/10.1103/tr6y-kpc6.

[17] R. Nagpal *et al.*, Journal of High Energy Astrophysics **47**, 100396 (2025), https://doi.org/10.1016/j.jheap.2025.100396.

[18] H. Chaudhary *et al.*, Journal of High Energy Astrophysics **50**, 100507 (2026), https://doi.org/10.1016/j.jheap.2025.100507.

[19] B. Ratra and P. J. E. Peebles, Phys. Rev. D **37**, 3406 (1988), doi:10.1103/PhysRevD.37.3406.

[20] C. Wetterich, Nucl. Phys. B **302**, 668 (1988), doi:10.1016/0550-3213(88)90193-9.

[21] R. R. Caldwell, R. Dave and P. J. Steinhardt, Phys. Rev. Lett. **80**, 1582 (1998), doi:10.1103/PhysRevLett.80.1582, arXiv:astro-ph/9708069.

[22] M. Chevallier and D. Polarski, Int. J. Mod. Phys. D **10**, 213 (2001), doi:10.1142/S0218271801000822, arXiv:gr-qc/0009008.

[23] E. V. Linder, Phys. Rev. Lett. **90**, 091301 (2003), doi:10.1103/PhysRevLett.90.091301, arXiv:astro-ph/0208512.

[24] A. G. Cohen, D. B. Kaplan and A. E. Nelson, Phys. Rev. Lett. **82**, 4971 (1999), doi:10.1103/PhysRevLett.82.4971, arXiv:hep-th/9803132.

[25] M. Li, Phys. Lett. B **603**, 1 (2004), doi:10.1016/j.physletb.2004.10.014, arXiv:hep-th/0403127.

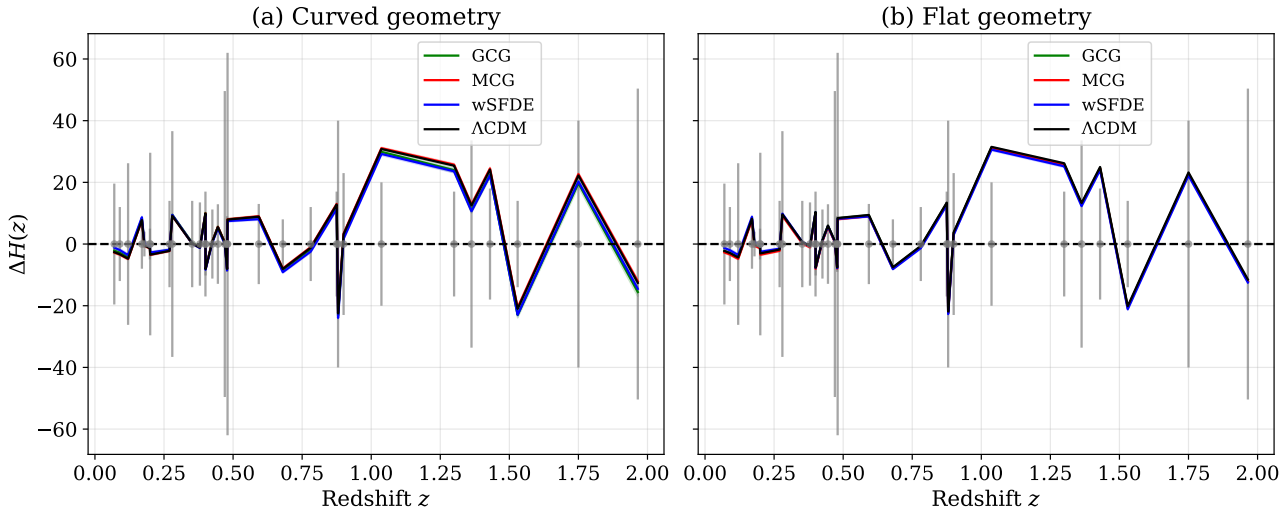


Figure 9: Residual evolution $\Delta H(z) = H_{\rm obs} - H_{\rm model}$ for the considered cosmological models using the combined dataset D_3. The left and right panels correspond to curved and flat geometries, respectively.

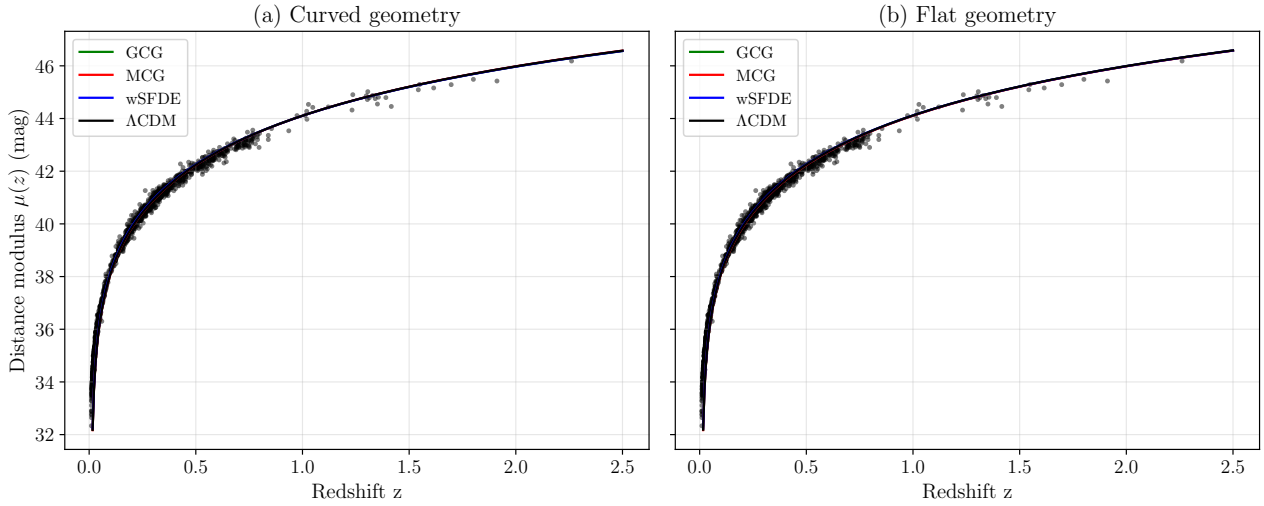


Figure 10: Evolution of the distance modulus $\mu(z)$ for different cosmological models using the combined dataset D_3. The shaded regions denote the 1σ confidence intervals obtained from the MCMC analysis.

[26] S. Wang, Y. Wang and M. Li, Phys. Rept. **696**, 1 (2017), doi:10.1016/j.physrep.2017.06.003, arXiv:1612.00345.

[27] A. Y. Kamenshchik, U. Moschella and V. Pasquier, Phys. Lett. B **511**, 265 (2001), doi:10.1016/S0370-2693(01)00571-8, arXiv:gr-qc/0103004.

[28] M. C. Bento, O. Bertolami and A. A. Sen, Phys. Rev. D **66**, 043507 (2002), doi:10.1103/PhysRevD.66.043507, arXiv:gr-qc/0202064.

[29] N. Bilic, G. B. Tupper and R. D. Viollier, Phys. Lett. B **535**, 17 (2002), doi:10.1016/S0370-2693(02)01716-1, arXiv:astro-ph/0111325.

[30] H. B. Benaoum, arXiv:hep-th/0205140.

[31] U. Debnath, A. Banerjee and S. Chakraborty, Class. Quant. Grav. **21**, 5609 (2004), doi:10.1088/0264-9381/21/23/019, arXiv:gr-qc/0411015.

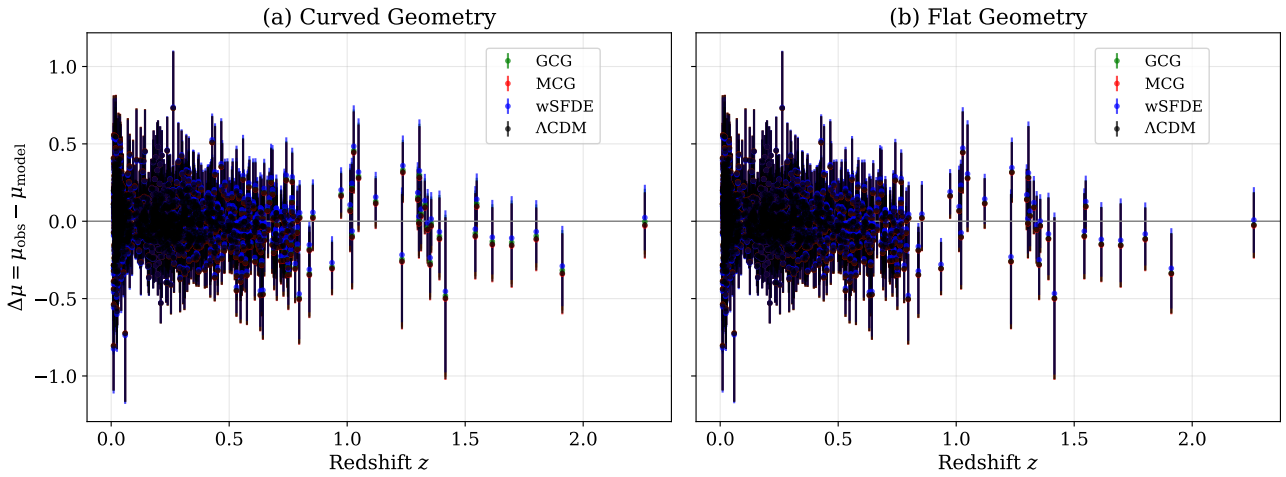


Figure 11: Residual distributions of the distance modulus, $\Delta\mu(z) = \mu_{\rm obs} - \mu_{\rm model}$, for the considered cosmological models using the combined dataset D_3 in curved and flat geometries.

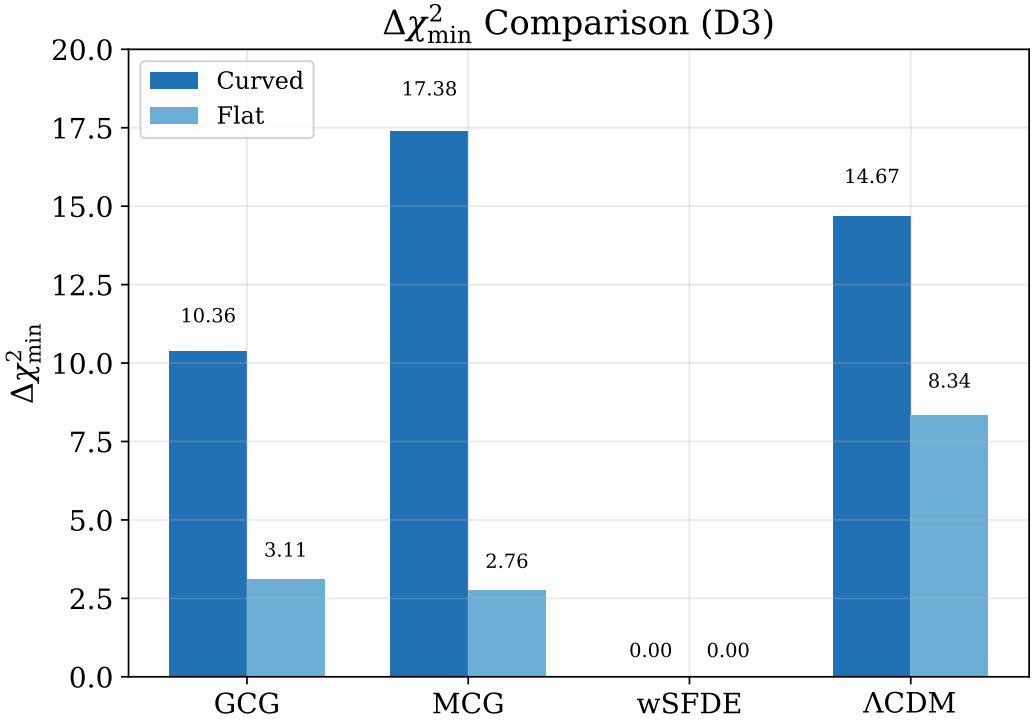


Figure 12: Comparison of the relative chi-square differences $\Delta\chi^2_{\rm min}$ for the GCG, MCG, wSFDE, and ΛCDM models using the combined dataset D_3 in curved and flat geometries.

[32] J. Lu, Y. Gui and X. Zhang, Eur. Phys. J. C **63**, 349 (2009), DOI:10.1140/epjc/s10052-009-1118-8.

[33] S. Nojiri and S. D. Odintsov, Phys. Rept. **505**, 59 (2011), doi:10.1016/j.physrep.2011.04.001, arXiv:1011.0544.

[34] T. Clifton, P. G. Ferreira, A. Padilla and C. Skordis, Phys. Rept. **513**, 1 (2012), doi:10.1016/j.physrep.2012.01.001, arXiv:1106.2476.

[35] S. Capozziello and M. De Laurentis, Phys. Rept. **509**, 167 (2011), doi:10.1016/j.physrep.2011.09.003, arXiv:1108.6266.

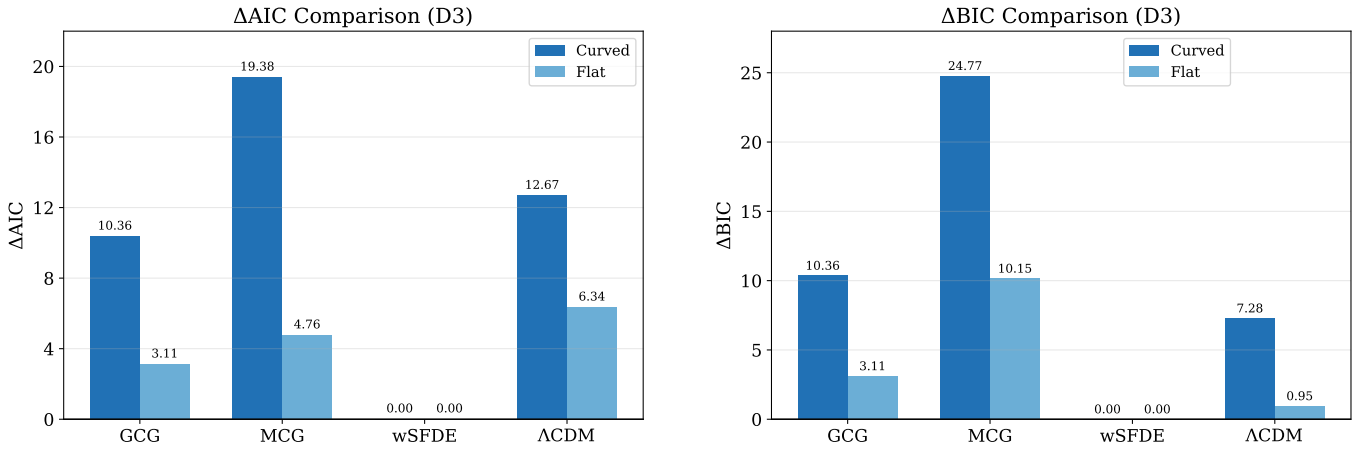


Figure 13: Comparison of the relative Akaike Information Criterion (ΔAIC) and Bayesian Information Criterion (ΔBIC) for different cosmological models using the combined dataset D_3 (PP + CC + DESI DR2 + CMB). The left panel represents the ΔAIC comparison, while the right panel shows the corresponding ΔBIC values. Smaller values indicate a statistically preferred model.

[36] M. O. Ribas, F. P. Devecchi and G. M. Kremer, Phys. Rev. D **72**, 123502 (2005), doi:10.1103/PhysRevD.72.123502, arXiv:gr-qc/0511099.

[37] G. M. Kremer and F. P. Devecchi, Phys. Rev. D **67**, 047301 (2003), doi:10.1103/PhysRevD.67.047301.

[38] B. Saha, Phys. Part. Nucl. **49**, 146 (2018), doi:10.1134/S1063779618020044.

[39] B. Saha, Phys. Rev. D **64**, 123501 (2001), doi:10.1103/PhysRevD.64.123501,

[40] M. Goray and B. Saha, Eur. Phys. J. C **85**, 1146 (2025), https://doi.org/10.1140/epjc/s10052-025-14895-3.

[41] M. Goray and B. Saha, Eur. Phys. J. C **86**, 19 (2026), https://doi.org/10.1140/epjc/s10052-025-15230-6.

[42] M. Goray and B. Saha, Nucl. Phys. B **1027**, 117468 (2026), https://doi.org/10.1016/j.nuclphysb.2026.117468.

[43] B. Saha, Zh. Eksp. Teor. Fiz. **167**(1), 49–58 (2025), https://journals.rcsi.science/0044-4510/article/view/285035.

[44] H. Akaike, IEEE Trans. Autom. Control **19**, 716 (1974), doi:10.1109/TAC.1974.1100705.

[45] G. Schwarz, Ann. Stat. **6**, 461 (1978), doi:10.1214/aos/1176344136.

[46] A. G. Walker, Proc. Lond. Math. Soc. **42**, 90 (1937), doi:10.1112/plms/s2-42.1.90.

[47] J. V. Narlikar, *Introduction to Relativity*, Cambridge University Press, New York (2010).

[48] D. Stern *et al.*, J. Cosmol. Astropart. Phys. **02**, 008 (2010), doi:10.1088/1475-7516/2010/02/008, arXiv:0907.3149.

[49] M. Moresco *et al.*, J. Cosmol. Astropart. Phys. **08**, 006 (2012), doi:10.1088/1475-7516/2012/08/006, arXiv:1201.3609.

[50] M. Moresco *et al.*, J. Cosmol. Astropart. Phys. **05**, 014 (2016), doi:10.1088/1475-7516/2016/05/014, arXiv:1601.01701.

[51] C. Zhang *et al.*, Res. Astron. Astrophys. **14**, 1221 (2014), doi:10.1088/1674-4527/14/10/002, arXiv:1207.4541.

[52] J. Simon, L. Verde and R. Jimenez, Phys. Rev. D **71**, 123001 (2005), doi:10.1103/PhysRevD.71.123001, arXiv:astro-ph/0412269.

[53] T. Delubac *et al.*, Astron. Astrophys. **574**, A59 (2015), doi:10.1051/0004-6361/201423969, arXiv:1404.1801.

[54] DESI Collaboration, Phys. Rev. D **112**, 083516 (2025).

[55] DESI Collaboration, Phys. Rev. D **112**, 083514 (2025), https://doi.org/10.1103/2wwn-xjm5, arXiv:2503.14739.

[56] D. Foreman-Mackey, D. W. Hogg, D. Lang and J. Goodman, Publ. Astron. Soc. Pac. **125**, 306 (2013), doi:10.1086/670067, arXiv:1202.3665.